Simple, controllable and environmentally friendly synthesis of FeCoNiCuZn-based high-entropy alloy (HEA) catalysts, and their surface dynamics during nitrobenzene hydrogenation

Márquez, Victor; Santos, Janaina S.; Buijnsters, Josephus G.; Praserthdam, Supareak; Praserthdam, Piyasan

Simple, controllable and environmentally friendly synthesis of FeCoNiCuZn-based high-entropy alloy (HEA) catalysts, and their surface dynamics during nitrobenzene hydrogenation

Victor Márquez [a], Janaina S. Santos [a], Josephus G. Buijnsters [b], Supareak Praserthdam [c], Piyasan Praserthdam [a,*]

[a] Center of Excellence on Catalysis and Catalytic Reaction Engineering, Department of Chemical Engineering, Faculty of Engineering, Chulalongkorn University, Bangkok 10330, Thailand
[b] Department of Precision and Microsystems Engineering, Research Group of Micro and Nano Engineering, Delft University of Technology, Mekelweg 2, 2628 CD Delft, the Netherlands
[c] High-Performance Computing Unit (CECC-HCU), Center of Excellence on Catalysis and Catalytic Reaction Engineering (CECC), Chulalongkorn University, Bangkok 10330, Thailand

ARTICLE INFO

ABSTRACT

High-entropy alloys (HEAs) have rapidly become one of the hottest research topics in several fields, including materials science, corrosion technology, and catalysis because of their multiple advantages and their potential applications. In this study, using a novel straightforward electroless deposition method, multi-elemental alloys (FeCoNiCuZn) supported on graphite were prepared with controlled metal loading (HEA/g-X; $X = 40, 80, 100$) without any high temperature post-treatments. These materials were characterized using scanning electron microscopy, transmission electron microscopy, energy-dispersive X-ray spectroscopy, X-ray photoelectron spectroscopy, and X-ray diffraction, and showed a composition ranging from 11 at.% to 31 at.% for each metallic element, a total metal loading varying from 1.3 to 5.2 at.% (5.9 to 21.5 wt.%), homogeneous distribution, and an amorphous structure. Electrochemical impedance spectroscopy, cyclic voltammetry, linear sweep voltammetry, and chronoamperometry were used to evaluate the surface dynamics and the effect of the solution pH during the electrochemical hydrogenation of nitrobenzene using the HEA/g-40 material. The nitrobenzene conversion (>9 $mmol_{NB}$ g_{cat}^{-1} h^{-1}) and aniline production (≈ 4 $mmol_{AN}$ g_{cat}^{-1} h^{-1}) rates in Na_2SO_4 solution (at -1.0 V vs. Ag/AgCl) demonstrated a strong dependence on the applied potential. After comparing the results in alkaline medium (KOH), a competitive adsorption of species (nitrobenzene and H_2O) was observed, showing a synergistic effect that greatly improved the selectivity of the nitrobenzene hydrogenation to aniline, from 23% in Na_2SO_4 to an outstanding 94% in KOH at the same applied potential, surpassing the results of a platinum electrode (34% in KOH). These results provide insightful information regarding the nature of the active sites involved in each step of the reaction mechanism, and gives useful means to develop new, tailored multifunctional HEA electrocatalyst materials.

1. Introduction

Climate awareness and environmental protection have gained momentum in the recent past and they have triggered the development of new and more efficient processes and materials [1–3]. Among others, this has led to the reevaluation of many traditional industrial-scale processes, in the pursuit of new renewable energy sources [4,5], lower consuming methods, and more efficient and stable catalysts. When it comes to the development of new materials, the use of non-metals [6–8] or non-noble metals [9–11] catalysts are two major trends currently involving a big volume of research for many different processes. Carbon-based materials represent an interesting group, thanks to the development of a wide variety of techniques to control their morphology and chemical composition, including carbon nanotubes [12–14], graphene-based compounds [15–17], carbon shells [18], graphitic carbon nitrides [19–22], among many other options. These diverse

morphologies and structures exhibit the intrinsic advantage of high surface area, good electrical and thermal conductivity, and high stability for reduction or hydrogenation processes [23,24].

On the other hand, multi-elemental alloys, with more than 4 elements as main elements or in equimolar combinations, are an attractive option due to their high mechanical and thermal stability such as high-temperature strength, wear resistance, high hardness, good structural stability, good corrosion and oxidation resistance, and relatively easy processing required for their synthesis and crystal phase control [25–27], which makes them promising candidates to be used as catalysts [28]. The so-called High-Entropy Alloys (HEAs) have the unique property of a multitude of active sites for different reactions owing to the independent interaction of each atom [29]. Other advantage of these metallic alloys is their intrinsic conductive nature, which makes them suitable candidates for electrocatalysis and provides an effective way to control the extent of the reaction as well as the energy input required. The HEAs are defined as alloys with a minimum of 5 elements, where all of the elements are considered majority (> 5 at.%), ideally in equimolar compositions, causing an increase in the mixing entropy (ΔS_{mix}). This equimolar composition (e.g. 20 at.% for each element) would produce the maximum increase of stability due to the entropy effect ($\Delta S_{mix} = 1.6R$, with R being the gas constant, $R = 8.3145$ J mol^{-1} K^{-1}). The minimum value to classify a material as high entropy, as reported initially by Yeh et al. [26] and later by Xu et al. [30] and Zhang et al. [31], is $\Delta S_{mix} = 1.5R$, which allows a variation of the elemental composition between 10 and 35 at.% as reported by Cantor et al. [25]. One of the consequences of this effect is the increase in the overall stability of the alloy materials due to the low diffusivity of constituent atoms [29].

The use of HEAs as catalysts is a relatively new practice [29], and most researchers have focused on the use of noble metal (e.g., Pt, Pd, Ir, Ru, Rh) [28,32] or non-noble metal (e.g., Fe, Mn, Cr, Co, Ni, Ti, Nb, V) [33,34] compositions, on the development of different synthetic methods [29,35,36], and on different catalyst morphologies. HEA catalysts have been explored in reactions like the hydrogen evolution reaction (HER) [37,38], oxygen evolution reaction (OER) [39], and oxygen reduction reaction (ORR) [40], where the stability of the material is considered as the main problem.

The selective hydrogenation of organic molecules, to obtain added value products, is a field where the HEAs present a remarkable advantage compared to the traditional alloys or metallic electrodes used as electrocatalysts. The multiplicity of active sites and the improved mechanical and chemical stability make the HEAs a promising technology for processes requiring long term operation and high selectivity. In this regard, we chose the hydrogenation of nitrobenzene as model system for catalytic selective hydrogenation to produce aniline because of the importance at industrial scale. Amines are important precursors in the plastics, medical, and pigments industries. Intense and extensive research has been devoted to the study of the electrocatalytic hydrogenation of nitro compounds using different methods like thermal catalysis [41–43], photocatalysis [44,45], and electrocatalysis [46,47]. Among these, electrocatalysis is the least studied and the one presenting more difficulties, especially regarding the conversion yields, selectivity, stability of the materials and scalability. A variety of materials and methods have been used to overcome these problems, and the best results have been obtained using copper (Cu) and its alloys [48,49], or alloys with noble metals (Pt, Pd) [50] in different morphologies. These electrocatalysts provide relatively large potential window and slow hydrogen evolution kinetics. However, the main drawback is the poor selectivity of the products and considerably low conversion efficiency ranging from 10 to 80%, with a strong dependence on the electrode material, the applied potential, the solvent used, and the pH of the solution [51].

To harvest the maximum benefits of the high-entropy condition, the metals combination is a fundamental parameter for successfully synthesizing the HEAs and controlling the catalytic activity of the materials. In this study, we addressed the hydrogenation of nitrobenzene by a five-element non-noble metal HEA electrocatalyst. By design, we selected Cu for its capacity to strongly adsorb hydrogen and make it available for hydrogenation reactions [52], Zn for the ability to adsorb anions and reduce the hydrogen evolution reaction [53], Ni and Co because of their high activity toward reducing protons and producing hydrogen adsorbed species in alkaline media [54], and Fe because of its well-known capacity to adsorb oxygen species, which improves the activity in alkaline media and improves the oxygen reduction reaction [55]. This combination of catalytic properties of each individual metal, mixed with their electronic and atomic similarities, covers all the properties required, theoretically, to achieve good hydrogenation results.

Herein, we present a simple and environmentally friendly method, based on electroless deposition, to synthesize FeCoNiCuZn-based HEAs on graphite support with control over the elemental composition. Physical and electrochemical methods were used to elucidate the dynamics of the adsorption of the species in solution (H$_2$O, nitrobenzene, H$^+$, aniline) on the catalyst surface, using the nitrobenzene molecule as a probe system for the hydrogenation process. Also, we present a discussion about the nature of the active sites and the important role of the adsorbed hydrogen species (-H) in the hydrogenation process, which can be used to design new catalysts with tailored properties to improve the efficiency of the electrocatalytic hydrogenation processes in solutions with different pHs.

2. Experimental methods

2.1. Chemicals

All chemical reagents used in the experiments were of analytical grade and used without further purification. The water used for preparing the solutions was de-ionized to achieve high resistivity (> 16 MΩ). The graphite used was obtained from compressed graphite bars with a 99.5% purity and a resistivity of 9 μΩ m (Sigma-Aldrich).

2.2. HEA synthesis

The high-entropy alloys were synthesized using an electroless deposition method [56–59], modified from the one reported elsewhere by Pandey et al. [60]. The graphite used as support was initially treated with concentrated boiling sulfuric acid (98%, Merck) for two hours, then rinsed and dried on a hot plate to evaporate the remains of sulfuric acid. A solution with a total metal concentration equal to 0.05 M, using an equimolar concentration of the precursor metals (i.e., C_{Fe}: C_{Co}: C_{Ni}: C_{Cu}: C_{Zn}), was prepared using Fe(NO$_3$)$_3$, Co(NO$_3$)$_2$, Ni(NO$_3$)$_2$, Cu(NO$_3$)$_2$ and Zn(NO$_3$)$_2$ (Sigma-Aldrich, analytical grade, > 95%, used without further purification). Different ratios of metals solution volume (S_M (mL)) versus the mass of graphite (g wt) (S_M/g wt: 40, 80, 120 (mL$_{solution}$/g$_{graphite}$)) were used, to evaluate the variation in metal loading. The mixture was stirred vigorously for 24 h. After this, the remaining solid was filtered, rinsed with DI water, and dried at 110 °C for 24 h before use. The solids were stored and labeled HEA/g-x (X: 40, 80, 120).

2.3. Electrodes preparation

An ink of HEA/g-X was prepared using 5 mg of HEA/g-X powder, 50 μL of Nafion® solution 5 wt.% in short-chain alcohols (Sigma-Aldrich), 750 μL of isopropanol (Sigma-Aldrich, > 99.5%), and 200 μL of DI water. The ink mixture was sonicated for 30 min in intervals of 5 min to ensure proper mixing. The mixture was sonicated for 5 extra minutes right before the preparation of the electrodes.

Graphite disks were treated with sandpaper #250, #400, and #600 grit to ensure homogeneous high roughness surface, then sonicated in isopropanol for 10 min, followed by sonication in water for 10 min to remove grease and left-over graphite powder. In the electrode preparation sequence, they were sonicated with isopropanol for 5 min and dried under air before adding 1 mL of HEA/g-x ink, which was dried

under air and finally dried at 80 °C in an oven for 2 h.

2.4. Materials characterization

The crystalline structure of the materials was analyzed by X-ray diffraction (XRD) using a Bruker D8 Advance with a Cu anode and Kα1 (1.544 Å) irradiation, a 2θ range from 10° to 80° and a scan rate of 0.02 °/min. The surface concentration and chemical state of the elements were measured using X-ray photoelectron spectroscopy (XPS) on a spectrometer AMICUS using Mg Kα X-ray radiation (1253.6 eV) and Al Kα X-ray radiation (1486.6 eV) at a voltage of 15 kV and current of 12 mA. Scanning electron microscopy (SEM) and energy-dispersive X-ray spectroscopy (EDX) were used to study the surface morphology of the catalysts and overall concentration of metals on the surface. For this, an AMICUS photoelectron spectrometer was used with an Mg Kα X-ray source controlled by KRATOS VISION2 software at a voltage of 10 kV and current of 20 mA. The binding energy value was calibrated by the C 1s peak at 284.6 eV, and the elements Fe 2 s (6.398 eV), Co 2 s (6.924 eV), Ni 2 s (7.471 eV), Cu 2 s (8.040 eV), and Zn 2 s (8.630 eV), respectively. Transmission electron microscopy (TEM) measurements were made using a JEOL JEM-2010 equipment on a Cu grid and the EDX spectra using an Oxford X-Max 80T accessory.

Electrochemical experiments were carried out using a potentiostat/galvanostat Autolab® PGSTAT204 and electrochemical impedance spectroscopy (EIS) experiments were performed using a frequency response analyzer (FRA32M) module with an A.C. perturbation of 10 mV, in the range of 100 kHz to 0.1 Hz at different applied potentials in the presence and the absence of nitrobenzene. Before each electrochemical experiment, the solution was deoxygenated with ultrapure (> 99.99%, Linde) N_2 for 30 min and the open-circuit voltage was measured to ensure a stable initial condition.

2.5. Nitrobenzene hydrogenation

The hydrogenation of nitrobenzene was carried out using an H-type cell with a solution volume of 40 mL. The compartments were separated by a Nafion® 115 membrane (Sigma-Aldrich) to ensure the ionic exchange while keeping the solutions separated. The counter electrode was a platinized titanium mesh (Anomet®) with a geometrical area of 6.3 cm^2. The reference electrode was a double compartment, Ti shielded Ag/AgCl (KCl 3 M) commercial electrode (Metrohm®). In the working electrode compartment, a solution of Na_2SO_4 (> 99%, Merck) (0.1 M, pH = 5), or KOH (> 85%, Univar) (1.0 M, pH = 14), and 400 μM concentration of nitrobenzene (Sigma-Aldrich) was used as support electrolyte under constant magnetic stirring to ensure homogeneous mixing. The solution used in the counter electrode compartment was prepared to match the concentration of support electrolyte used in the working electrode compartment, namely Na_2SO_4 (0.1 M) or KOH (1.0 M), respectively. The concentrations of nitrobenzene and aniline in aqueous solution were measured on a LAMBDA 650 UV/Vis spectrophotometer using deconvolution to calculate the absolute concentrations.

3. Results and discussion

3.1. Materials characterization

The surface morphology of the synthesized catalysts was analyzed using SEM. Fig. 1 depicts the micrographs of the material prepared with the three different compositions. The images show that all three materials exhibit similar morphology, corresponding to the laminar structure of the graphite substrate. The alloy particles were not observed due to their small size, product of the low metal loading and the procedure used. The sheet-like structure of the graphite support ensures a high specific surface area available for the adsorption and homogeneous distribution of the alloy particles.

The distribution of the elements is shown in SEM-EDX results of the HEA materials (Figs. S1–3), where the five elements of interest (Fe, Co, Ni, Cu, and Zn) are present in the surface of the catalysts in a fairly homogeneous distribution. Fig. 2 depicts the TEM results for the HEAs. It is important to remark that no clumping, individual metal clusters, or areas could be found. This implies that the probability of each metal interacting with the others is increased, and the segregation of the individual phases was avoided as shown in Fig. 2a,d for the lowest metal loading (HEA/g-40), while the materials with higher metal loadings
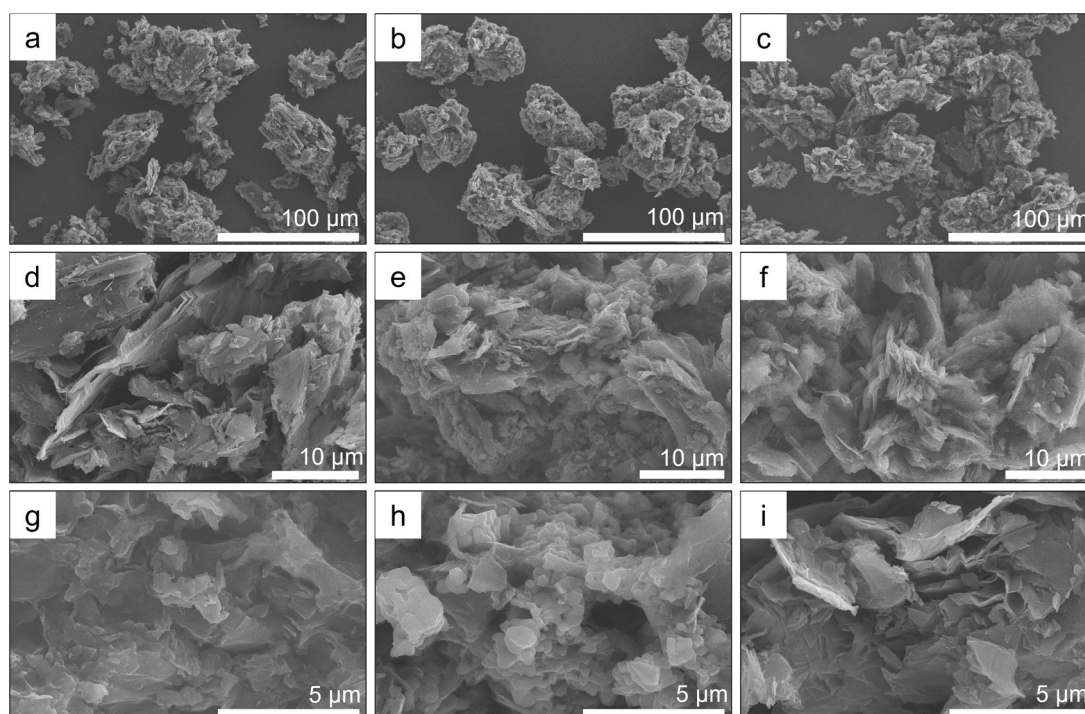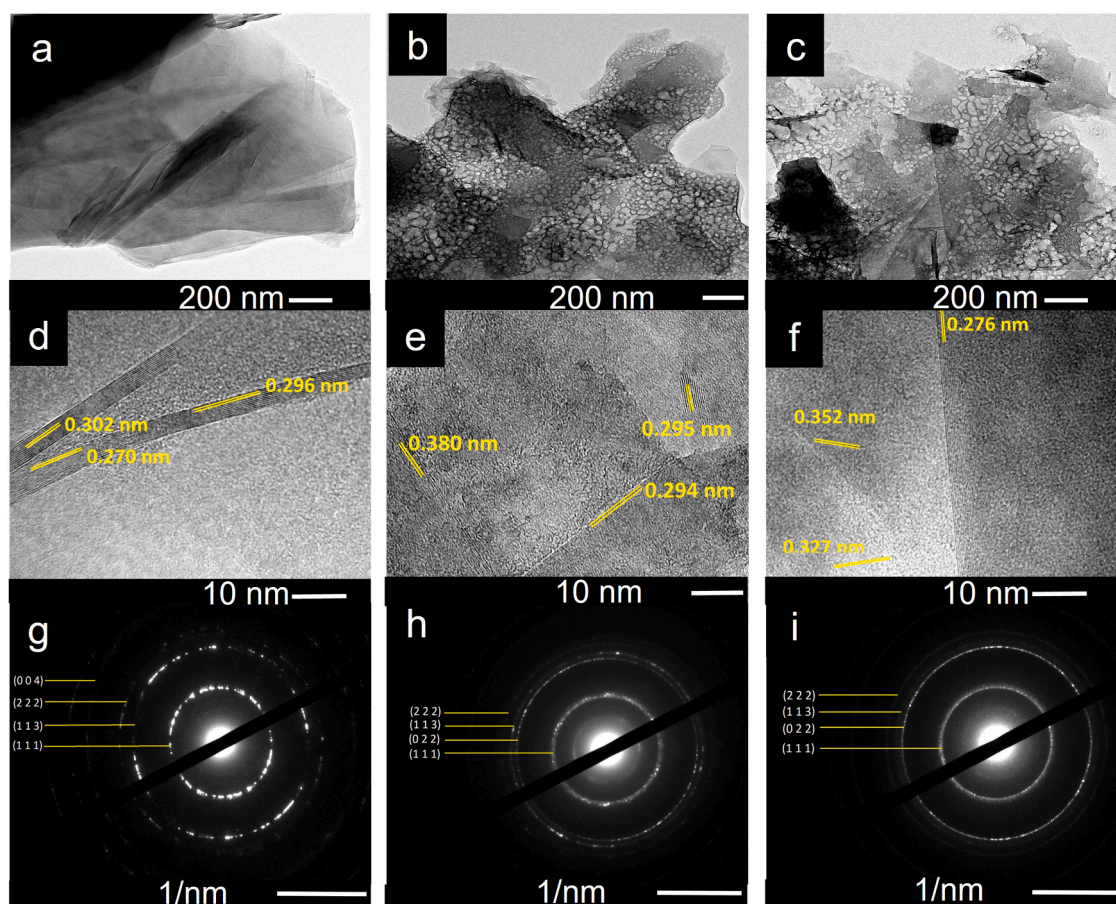

Fig. 1. SEM images with different magnifications of the three catalysts synthesized. (a,d,g) HEA/g-40; (b,e,h) HEA/g-80; (c,f,i) HEA/g-120.

Fig. 2. TEM results for the synthesized HEAs. (a,d,g) TEM image, interplanar distance, and pattern SAED for HEA/g-40, (b,e,h) HEA/g-80, and (c,f,i) HEA/g-120, respectively.

present phase segregation as seen in Fig. 2b,e and Fig. 2c,f for the HEA/g-80 and HEA/g-120, respectively. In Fig. 2d-f, it can be seen how the interplanar distance of the films increases with the metal loading going from an average of (0.29 ± 0.03) nm in the HEA/g-40 to (0.38 ± 0.03) nm for HEA/g-80 and (0.33 ± 0.03) nm for HEA/g-120. This is most likely caused by the increase in the relative content of Zn in the whole materials as reported by Huang et al. [61]. The difference in atomic size and crystal structure of Zn (hexagonal packed HCP) with the other elements Fe (BCC or FCC), Co (HCP), Ni (FCC), Cu (FCC) and the lack of empty orbitals on the D-level cause an increase in the structural stress, increase of interplanar distances, shifting to lower diffraction peaks' angles and a modification of the lattice constant [62,63].

The elemental composition of the three materials is presented in Table 1 (for more detailed information regarding the elemental composition see Tables S1–3 in the Supplementary Material), where it is shown that the ratio of mass of graphite support-to-volume of solu-

Table 1
Elemental compositions of the catalysts prepared using different weight/solution ratios obtained by EDX.

Element	HEA/g-40		HEA/g-80		HEA/g-120	
	wt.% (±0.1)	at.% (±0.1)	wt.% (±0.1)	at.% (±0.1)	wt.% (±0.1)	at.% (±0.1)
C	93.7	98.6	81.7	95.8	78.5	94.8
Fe	1.0	0.2	2.4	0.6	6.7	1.8
Co	0.8	0.2	3.8	0.9	3.0	0.7
Ni	1.0	0.2	3.5	0.8	3.3	0.8
Cu	1.5	0.3	4.0	0.9	4.0	0.9
Zn	1.9	0.4	4.6	1.0	4.5	1.0
Metals	6.3	1.3	18.3	4.2	21.5	5.2

allowed to effectively control the total metal loading. Additionally, the low concentration of the employed solution allowed the formation of thin films which crystallization and growth were controlled by the thermodynamics of the process favoring the formation of single-phase multi-elemental alloys or HEAs at lower loadings and multi-phase films for the higher metal loadings [26]. This was confirmed by the selected area electron diffraction (SAED) measurements. In Fig. 2g-i, the SAED patterns for the three materials correspond to a cubic structure, more specifically a magnetite-like structure (*Fd* −3 m) due to the relatively high amount of iron in the sample and the oxidation of the surface. In the case of the HEA/g-40, a polycrystalline structure was observed on the SAED, while for the other two materials the diffuse circles are evidence of amorphous characteristics. All the desired elements were detected by EDX measuments from the TEM selected area, with the relative concentrations given in supplementary materials (Table S4).

As mentioned before, one of the parameters to determine if a material can be classified as high-entropy alloy is the value of ΔS_{mix}. If this value is above the mark of 1.5R, the entropy effect is considered high enough to overcome the enthalpy of the mix and the material can considered to be entropy stabilized, using the following equation:

$$\Delta S_{mix} = -R\sum_i x_i \ln(x_i) \tag{1}$$

where x_i is the mole fraction of each element and R is the gas constant (R = 8.3145 J mol^{-1} K^{-1}).

Fig. 3 shows the individual contribution of each element in the three samples to the entropy of the mix using the concentrations obtained from EDX measurements (Table S4), and it shows how the ΔS_{mix} of the materials fall within the range of high entropy stabilized materials [26,
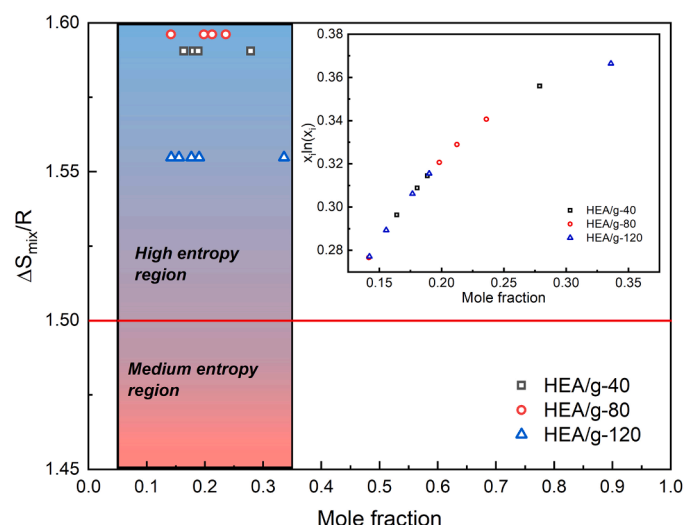
Fig. 3. ΔS_{mix} calculated for the synthesized materials. Insert: contribution to the ΔS_{mix} of each element as a function of the composition.

30,64]. It is important to notice that the contribution of each component increases steeply in the mole fraction range from 0.05 reaching a maximum value at $x_i = 0.35$, and after $x_i > 0.4$ the contribution to the entropy decreases sharply until it becomes zero when $x_i = 1$ shown in Fig. 3. This is the reason why increasing the concentration of a single element beyond this value ($x_i = 0.35$) has a negative effect on the contribution to the entropy of the mix.

To further examine the surface of the catalysts, XPS analysis was performed, as shown in Figs. S4–6 (see Supplementary Material) for the three different HEA/g-x materials. The wide scan shows two major edge signals, one at 280 eV corresponding to the C edge and a second one at 524 eV corresponding to the O edge. When it comes to the signals of the metals, the specific edge signals (719 eV (Fe); 790 eV (Co); 870 eV (Ni); 952 eV (Cu) and 1020 eV (Zn)) were within the noise level of the measurements and the oxidation states could not be analyzed. These results are a consequence of the low concentration of each metal on the catalyst (≈ 1 at.%, see Table 1), the matrix effect of the sample, and possible interactions between elements that can cause the loss in the detection sensitivity [65–68]. The analysis of the C signal (for example, see Fig. S4g for the HEA/g-40 material) provides useful information. It shows the main signal corresponding to the C—H bond (285 eV) caused by the exposed edges of the graphite sheets, like the functionalization of graphene sheet edges. The other three signals at 286.1 eV, 287.1 eV, and 288.3 eV are attributed to the oxygenated groups C—O, C═O and C—OOH, respectively. These oxygenated groups were expected as a result of the pretreatment of the graphite support prior to the alloys deposition, and have an important role in the electric performance of the catalysts, since these oxygenated functional groups may improve the dispersion of the substrate [69], the amount of surface defects and adsorption sites [70,71], and may enhance the electrical conductivity of the laminar graphite structures [69]. The signal at 284 eV was attributed to the C═C bond in the graphite sheets. The semi-quantitative analysis obtained by XPS for the HEA/g-40 material (see Supplementary material Table S1 for details) showed elemental compositions in the range of 5.6–11.0 wt.%, while compositional data derived from SEM-EDX vary from 0.8 to 1.9 wt.%. The considerable difference between XPS and SEM-EDX data arises from the difference in penetration depth of each technique [65], i.e. relatively higher wt.% are obtained by XPS as a result of its smaller penetration depth. On the other hand, the E/Mt data (i.e., ratio of each individual element to the sum of all the metals) show near-equimolar compositions (~0.20) for each of the synthesized materials (Tables S1–S3 in Supplementary Material). This is clear evidence of the formation of high-entropy alloys as the (metallic) elemental

composition falls well within the defined range of 10–35 at.% [59].

When it comes to multi-elemental alloys or high-entropy alloys, the phase of the material is a critical parameter, since it can cause different responses in the activity of the catalysts, as well as the selectivity and stability in different experimental conditions. The XRD results (Fig. 4) of the samples show a major signal corresponding to the characteristic peak of the graphite (0 0 2) plane at 26°. This signal tends to be a sharp peak for pristine graphite. In the HEA/g-x materials, the peak exhibits a broader shape, which is most likely the result of a modification of the inter-layer distance distribution, causing the broadening. This result is the consequence of two factors; first, the pre-treatment applied to the graphite to activate it, and second, the insertion of the HEA particles in the interlayer zones distorting the crystal structure, without breaking it. The smaller signal around 43° corresponds to the (1 0 0) plane and shows a similar broadening as the main peak. The third and smallest signal at 54° corresponds to the (0 0 4) peak from the graphite structure. The signal present at 45° was attributed to the (1 1 1) plane of the FCC structure of the HEA (FeCoNiCuZn), as reported by Huang et al. [61] and is consistent with the results obtained from the SAED measurements showing a cubic structure (Fig. 2g-i). It must be noted that this structure was obtained by direct electrochemical reduction without annealing treatments. The crystallite size calculated using the Scherrer's equation, gave an approximate size of (5 ± 1) nm.

3.2. Electrochemical characterization

3.2.1. Linear scan voltammetry

To further study the elemental distribution and presence of different phases or metal segregations, linear scan voltammetry (LSV) was carried out in alkaline media. The reduction of the different oxide species present on the surface was examined. Fig. 5 shows the electrochemical response of the three synthesized materials. For samples HEA/g-80 and HEA/g-120, a single broad signal was observed at −0.5 V (as indicated by arrow *a*), where the reduction of surface oxides (−0.5 V) and water reduction ((−1.0 V) signals overlapped, causing the loss of a well-defined peak for each process, and producing a current increase and reaching a quasi-steady-state until −1.4 V where hydrogen evolution took place and the current increased exponentially. This single signal showed that there is no metal segregation, as confirmed previously by SEM-EDX. In the case of the catalyst HEA/g-40, the signal showed two distinct peaks, the first at −0.5 V (*a*) and the second at −1.0 V (*b*), and finally, the hydrogen evolution reaction took place at −1.6 V (*c*). In this case, these two peaks were attributed [72–77] to the reduction of the surface oxide and the adsorption of water (according to the Volmer mechanism) before the massive hydrogen evolution. Following these
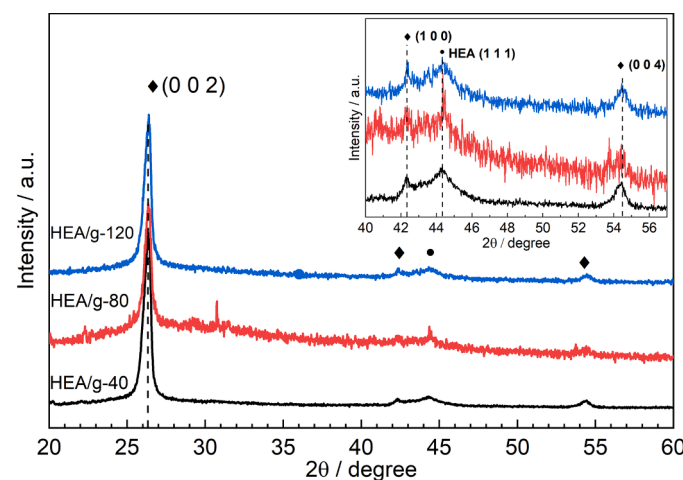

Fig. 4. XRD scan of the synthesized materials including peak identification. (□) Graphite signals (●).
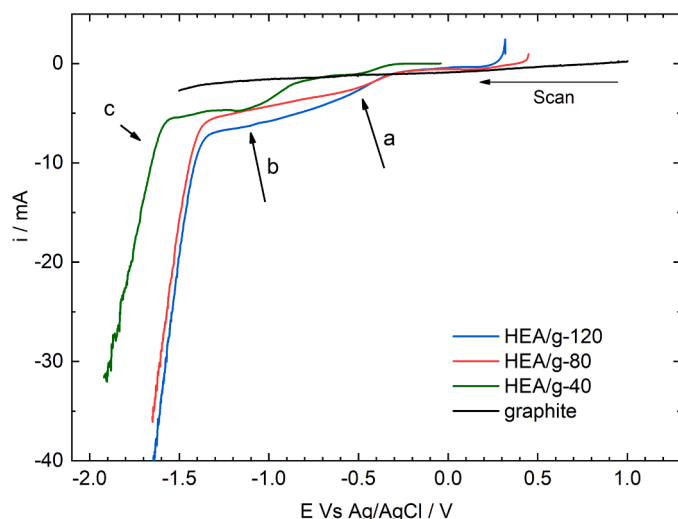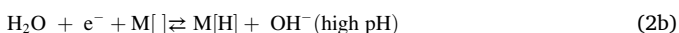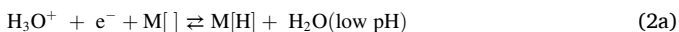
Fig. 5. Linear scan voltammetry of the three synthesized materials and unloaded graphite support in 1.0 M KOH (pH 14), scan rate 1 mV s^{-1}.

results, the material HEA/g-40 was selected to analyze the effect of pH on the behavior of the electroactive sites and the effect of nitrobenzene adsorption on the surface dynamics. The criteria to choose this material were two-fold, namely the separation of the reduction signals allowing a more comprehensive analysis and the wider potential window compared with the other two synthesized materials, which allows the study of the surface without the interference of the massive hydrogen evolution.

### 3.2.2. Electrochemical hydrogen transfer

The electrocatalytic hydrogenation processes usually involve the Hydrogen Evolution Reaction (HER) as a first step to produce the hydrogen required for the reaction to take place, but it can also be a competitive pathway reducing the Faradaic efficiency of the processes and affecting the selectivity of the reaction.

The electrochemical HER has been widely studied in acid and alkaline media. The commonly accepted mechanisms Volmer-Tafel [78,79] and Volmer-Heyrovsky [78,80] involve a series of chemical and electrochemical steps, which are normally used to characterize the catalytic behavior of different electrodes. First step is usually described by the Volmer equation, which involves the adsorption of the precursor species and depends on the pH of the solution, according to Eq. (2a-b).-:

$$H_3O^+ + e^- + M[\ ] \rightleftarrows M[H] + H_2O (low\ pH) \qquad (2a)$$

$$H_2O + e^- + M[\ ] \rightleftarrows M[H] + OH^- (high\ pH) \qquad (2b)$$

where M[] represents an adsorption site on the surface.

Once the Volmer reaction takes place, the adsorbed hydrogen species M[H] (or -H) are the precursors of the gaseous hydrogen (H$_2$). In this regard, two mechanisms can occur simultaneously, i.e., the Tafel reaction, a chemical step where two adsorbed species recombine to produce H$_2$ (Eq. (3)), and the Heyrovsky mechanism, an electrochemical step involving the concerted interaction between an adsorbed atom of hydrogen, another proton (or water molecule), and the transfer of a second electron (Eq. (4)):

$$M[H] + M[H] \rightleftarrows H_{2(g)} + 2M[\ ] \qquad (3)$$

$$M[H] + H_3O^+ + e^- \rightleftarrows H_{2(g)} + M[\ ] + H_2O_{(l)} \qquad (4)$$
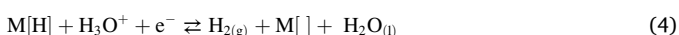
The combination of Eqs. 2 - 3 and Eqs. 2 - 4 are known as the Volmer-Tafel and Volmer-Heyrovsky mechanisms, respectively. These reactions have been widely studied on ideal surfaces (Pt, Pd) and many other surfaces including heterostructures and mixed materials [81,82], and provide useful information regarding the mechanisms or possible

pathways followed during the HER or the hydrogen transfer reactions (HTR).

3.2.3. Electrochemistry in acidic medium (Na$_2$SO$_4$)

Fig. 6a depicts the cyclic voltammetry data of the HEA/g-40 electrode in 0.1 M Na$_2$SO$_4$ (pH 5). At slow scan rates (5 – 10 mV s^{-1}), a reduction signal was observed at −0.5 V, corresponding to the surface oxide reduction. When the scan rate increased (50–500 mV s^{-1}), the signal shifted to 0 V and a strong capacitive behavior was observed. This high capacitance was caused by the roughness and porosity of the electrode. It can be noted that there is an oxidation signal at 0.6 V followed by the oxygen evolution signal after 1.0 V. The oxidation signal was attributed to the oxidation of the metallic surface. According to Löffler et al. [83], the broad nature of this signal can be related to the multiplicity of metals in the surface and their interactions. This behavior is characteristic for metallic alloys and supports the argument that the electrode is a solid-state solution [83,84]. In the case of metals segregation, the oxidation region would be composed of different individual peaks. The presence of surface oxides has been widely reported [85–87] to act as promoters to the oxygen evolution reaction (OER), or the oxygen transfer reaction (OTR). When the potential scan was performed at a slower scan rate (1 mV s^{-1}) in the reduction direction, starting from the open circuit potential, the reduction signal at −0.3 V seen only in slow scan rates got more defined (Fig. 6b). This shows that there was a diffusion-controlled process between −0.3 and −0.7 V, according to the Nicholson-Shain model, where the current of the peak is a linear function of the square root of the scan rate (see supplementary information Fig. S7):

$$i_p = \left(2.69x10^5\right)n^{3/2}AD_0^{1/2}C_0^*v^{1/2} \qquad (5)$$

Where i$_p$, n, A, D$_0$, C$_0$ and v are the peak current, number of electrons transferred, area of electrode, diffusion coefficient, concentration of the species and scan rate, respectively.

After that, the current increased with the potential until −1.5 V. This was attributed to the diffusion of the protons inside the porosity of the material, and the adsorption on the surface by atomic hydrogen, blocking the electroactive sites and increasing the resistivity of the surface [88,89]. Finally, at −1.7 V the massive hydrogen evolution process took place.

To analyze the surface coverage and the effect of the applied potential, electrochemical impedance spectroscopy (EIS) was used by applying an AC perturbation of ΔE = 10 mV. The Nyquist plots collected at different applied potentials are shown in Fig. 6c (See Fig S8 for more detail on the high frequency region), and the results were compared to an (R(RQ)) equivalent circuit [90]. The values for charge transfer resistance (R$_{ct}$) and capacitance (C) are shown in Fig. 6d, where a progressive increase in the capacitance of the electrode was observed from −0.5 V, reaching a maximum value at −1.5 V and decreasing steeply at −2.0 V. This trend, combined with the linear sweep voltammetry results, indicates a strong adsorption and high coverage of the surface of the electrode as a function of the applied potential [88,89]. This strong adsorption occupies the available electroactive sites causing an increase in the surface concentration of hydrogen. However, the recombination of these H atoms is slow, which means they are available to be transferred to different organic molecules, thus increasing the possibility of controlled hydrogenation processes. When the applied potential is more negative than −1.5 V, the energy is enough to activate the adsorbed hydrogen atoms and generate the massive hydrogen evolution. This may be the cause of the sharp decrease in the capacitance of the electrode due to the decrease in the surface concentration of H atoms. This decrease in the surface concentration and increase in the hydrogen evolution is also promoted by a decrease in the charge transfer resistance as a function of the applied potential (Fig. 6d), which reaches a lowest value at −2.0 V. The combination of high hydrogen coverage and low charge transfer resistance makes the applied potential of −1.5 V a convenient electrical
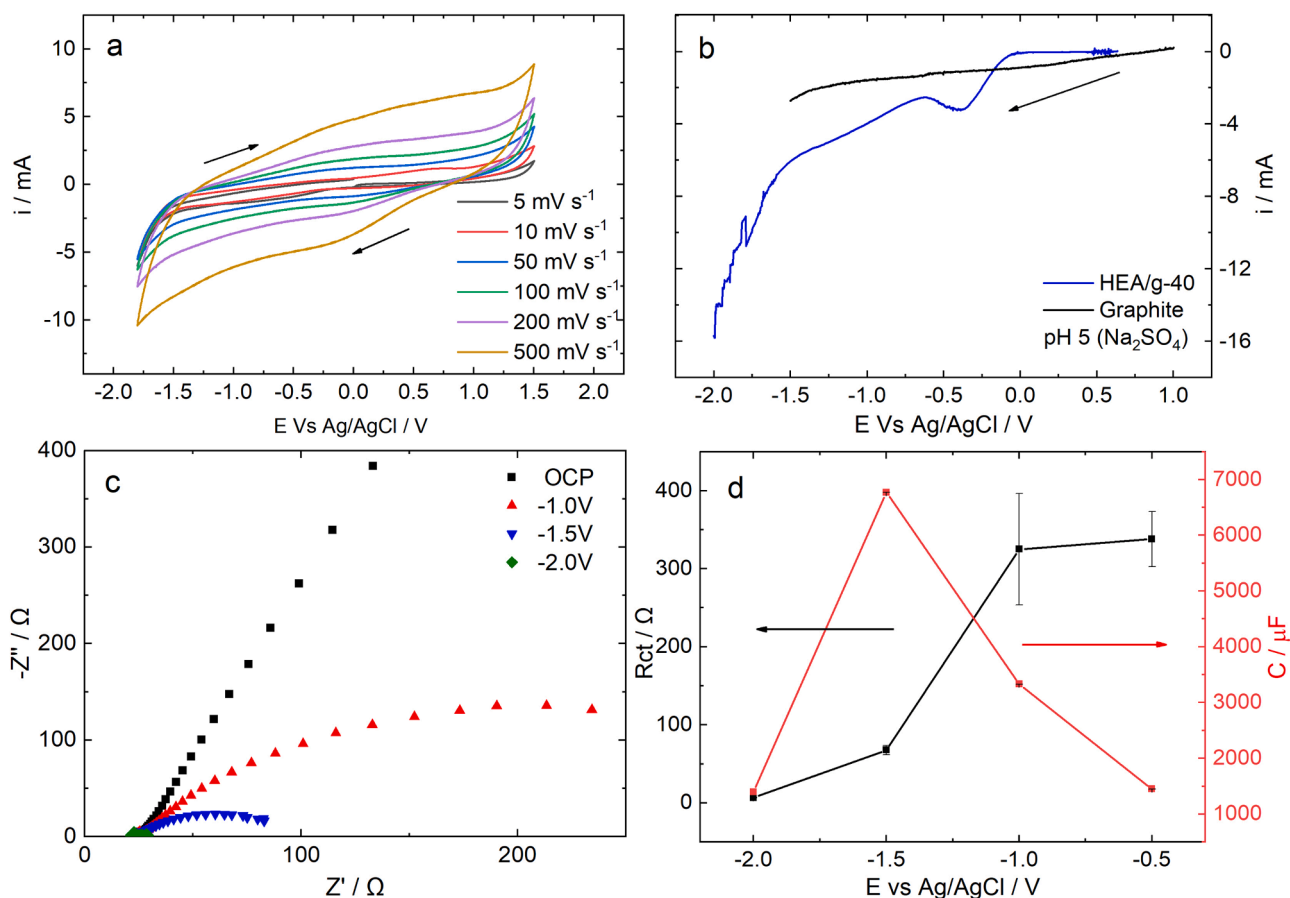
Fig. 6. Electrochemical behavior of HEA/g-40 electrode in 0.1 M Na_2SO_4 (pH 5). (a) Cyclic voltammetry at different scan rates. (b) Potential scan in the cathodic direction with linear scan rate of 1 mV s^{-1}. (c) Nyquist plots collected at different applied potentials. (d) R_{ct} and C as a function of applied potential calculated from the Nyquist plot using an equivalent circuit.

condition when it comes to the catalysis of the hydrogen transfer reaction because it promotes a hydrogenation process with low participation of the hydrogen evolution [88,89].

The afore-mentioned maximum in the capacitance due to hydrogen adsorption can be used as a boundary value to control the products obtained. At potential values below this maximum, the extensive hydrogenation products were not favored, and any direct reduction products were be obtained favorably. On the other hand, at more negative potential values (i.e., beyond the maximum value), the extensive production of hydrogenation products was improved, but at the cost of a lower Faradaic efficiency due to the strong activation of the H_2 evolution.

3.2.4. Electrochemistry in alkaline medium (KOH)

The same approach was used to analyze the electrochemical behavior of the HEA/g-40 electrode in alkaline medium (KOH, pH 14). It has been reported that high-entropy alloys can present activities comparable to Pt when used for hydrogen evolution in highly alkaline media [91]. Results strongly depend on the composition of the alloy and the synthesis method, and their activity is much more difficult to understand and model due to the multiplicity of possible active sites and their behavior as a function of the pH. In Fig. 7a, the cyclic voltammetry data of the HEA electrode shows a behavior completely different from the results obtained at acidic pH. In this case, two clearly defined reduction signals were present (−0.49 V and −1.0 V), which were attributed to the reduction of the surface oxides and the adsorption/reduction of water molecules [83]. In the positive direction scan, a single but wide signal with a maximum at −0.4 V extended between −1.0 V to 0.2 V approximately. This type of signal is characteristic of multi-elemental alloys

where many possible surface oxides can be produced due to the multiplicity of metallic atoms and surrounding environments. Furthermore, the fact that only one peak was seen on that region means that there was a solid solution and there was no metals segregation. A final peak was present at 0.5 V, which is characteristic of Ni and Co alloys due to the formation of the oxo-hydroxide surface species (NiOOH and CoOOH) which have been reported [92] as intermediates for the oxygen evolution reaction in this kind of metals and as important reactive species in electrochemical direct oxidation processes. When it comes to the hydrogen evolution/transfer process, the HEA electrode presented a high overpotential for the reaction to take place (Fig. 7b, below −1.5 V). This gave a broad working window making it possible to tune the desired products obtained by means of controlling the applied potential.

The impedance experiments in alkaline medium (Fig. 7c-d) (See Fig S9 for more detail on the high frequency region) showed an increase in surface capacitance (C) with a maximum value at −1.0 V, which corresponded to the position of the second reduction peak seen in the cyclic voltammetry and the linear scans. These results imply that the adsorption of water molecules was hindered by the presence of surface oxides, which also explains the dramatic reduction of the charge transfer resistance (R_{ct}), at −1.5 and −2.0 V, once the oxides were reduced (Fig. 7d). When the reduction process was completed after −1.0 V the metallic surface was exposed, and the adsorption reached a maximum value [88,89]. This surface concentration of adsorbed water molecules decreased at −1.5 and −2.0 V. The decrease in the surface concentration was attributed to the activation of the hydrogen evolution process, which did not seem to be strongly affected by the applied potential between −1.0 V and −1.5 V [88]. This means the process followed the Volmer-Tafel mechanism, and after −1.5 V the current increases
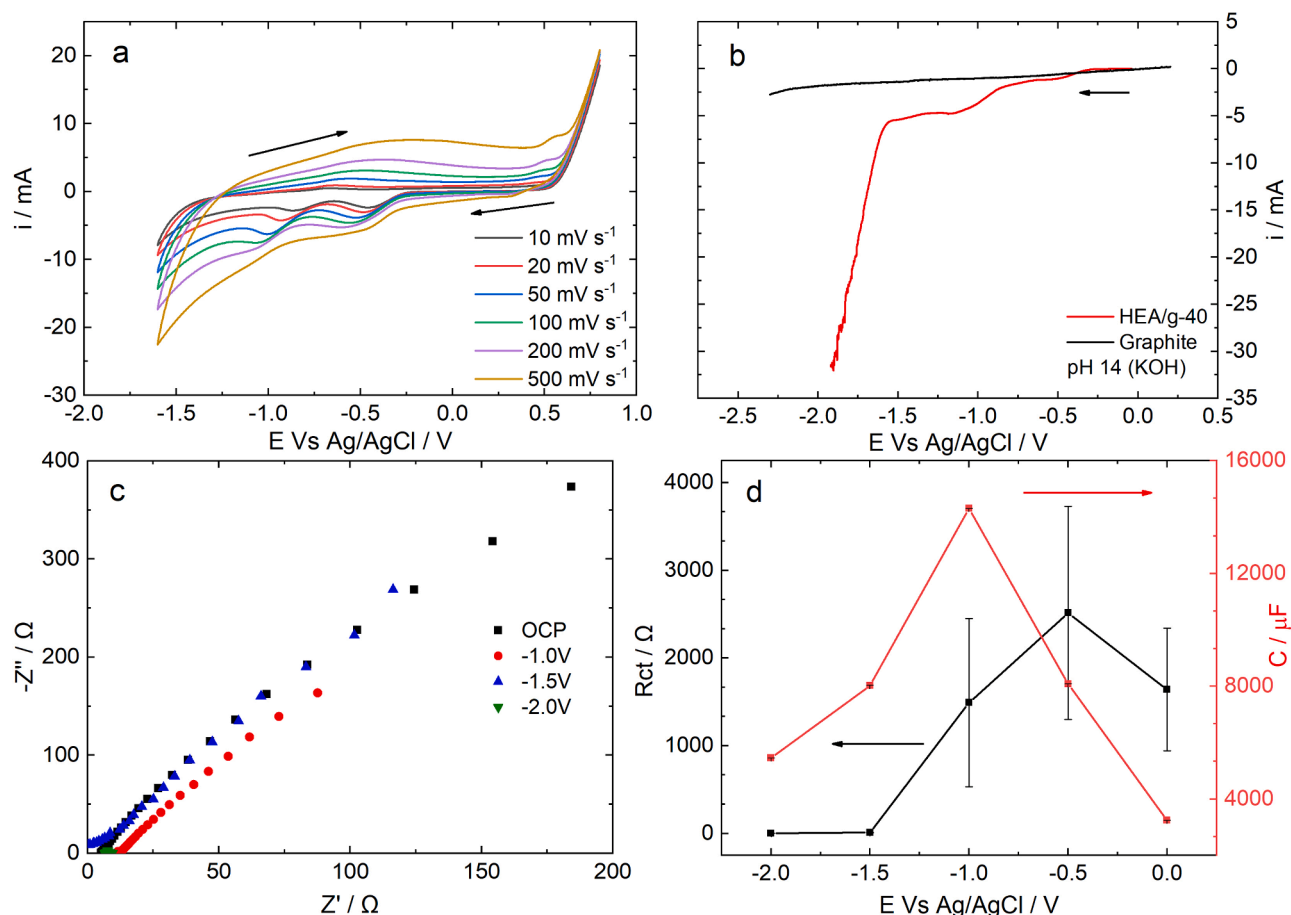
Fig. 7. Electrochemical behavior of HEA/g-40 electrode in 1.0 M KOH (pH 14). (a) Cyclic voltammetry at different scan rates. (b) Potential scan in the cathodic direction with linear scan rate of 1 mV s^{-1}. (c) Nyquist plots collected at different applied potentials. (d) R$_{ct}$ and C as a function of applied potential calculated from the Nyquist plot using an equivalent circuit.

exponentially with the applied potential (Fig. 7b), and the Volmer-Heyrovsky mechanism became dominant. Because of this, the surface concentration of hydrogen (or water in alkaline pH) was considerably reduced, caused by these reactions taking place simultaneously.

The dependence of the electrochemical behavior of the HEA electrode on pH is fundamental to properly understand and use them as catalysts when hydrogen or oxygen evolution reactions are involved. In Fig. 8a, the cyclic voltammetry scans obtained at different pH are compared. The activity at alkaline pH (i.e., in KOH) was higher for both hydrogen evolution and oxygen evolution, showing a stronger interaction between water molecules and the surface. In the case of hydrogen, the onset potential for massive H$_2$ evolution was located after the second reduction signal (−1.1 V), while for acid medium (i.e., Na$_2$SO$_4$) the H$_2$ evolution started after −1.5 V and with a lower current than for the alkaline medium. This could be explained by a strong interaction between the protons and the surface, a behavior consistent with that reported for Cu electrodes [50], where the surface adsorption energy is considerably high thus stabilizing the adsorbed hydrogen species (-H) and reducing the effect of the applied potential, and slowing down the kinetics of the hydrogen evolution (Volmer-Tafel mechanism). In the case of the basic medium, the hydrogen promoting species was not the proton (H$^+$), but the adsorbed water molecule (-OH$_2$), which adsorbs rapidly once the surface oxides were reduced, and reacted with a much stronger dependence on the potential than in acidic pH (Volmer-Heyrovsky mechanism).

One of the causes for the drastic change in the electrochemical behavior as a function of the pH of the solution was the formation of the

surface oxides, which enhanced the affinity of the surface to water molecules and therefore the oxygen evolution kinetics. It is important to notice that the oxygen evolution region showed a pronounced onset near 0.5 V in alkaline solution, whereas, in acid solution, the surface was less susceptible to oxidation, and therefore the oxygen evolution kinetics were much slower. A similar behavior was observed in the reduction region (Fig. 8a), where the electrode showed poor activity towards hydrogen evolution in Na$_2$SO$_4$ solution even at considerably high overpotentials ($\eta > -1.0$ V). In this regard, strong adsorption of protons in the surface, and high stability promoted by Cu and Zn [52] limits the hydrogen evolution. On the contrary, in alkaline medium, the reduced surface had also strong adsorption of water molecules, which were easily activated and catalyzed the massive hydrogen evolution after smaller overpotentials ($\eta > -0.5$ V). To properly evaluate the effect of the overpotential on the hydrogen evolution reaction and its availability toward transferring to other organic molecules for hydrogen transfer reaction (HTR), the linear scan voltammetry was plotted in the reversible hydrogen potential scale (Fig. 8b), as given by Eq. (6):

$$E_{RHE} = E_{electrode} + E^0_{Ag/AgCl} + 0.059pH \qquad (6)$$

In the hydrogen scale, the higher activity of the HEA electrode in alkaline medium was expected. The fact that the reduction signal at −0.1 V in both cases matches perfectly, means that the hydrogen (or water) adsorption takes place rapidly once the surface is completely reduced thereby exposing the metallic surface, and the subsequent hydrogen evolution.

In Fig. 8c, the impedance results show that at lower pH the charge transfer resistance was much smaller since the hydrogen reduction
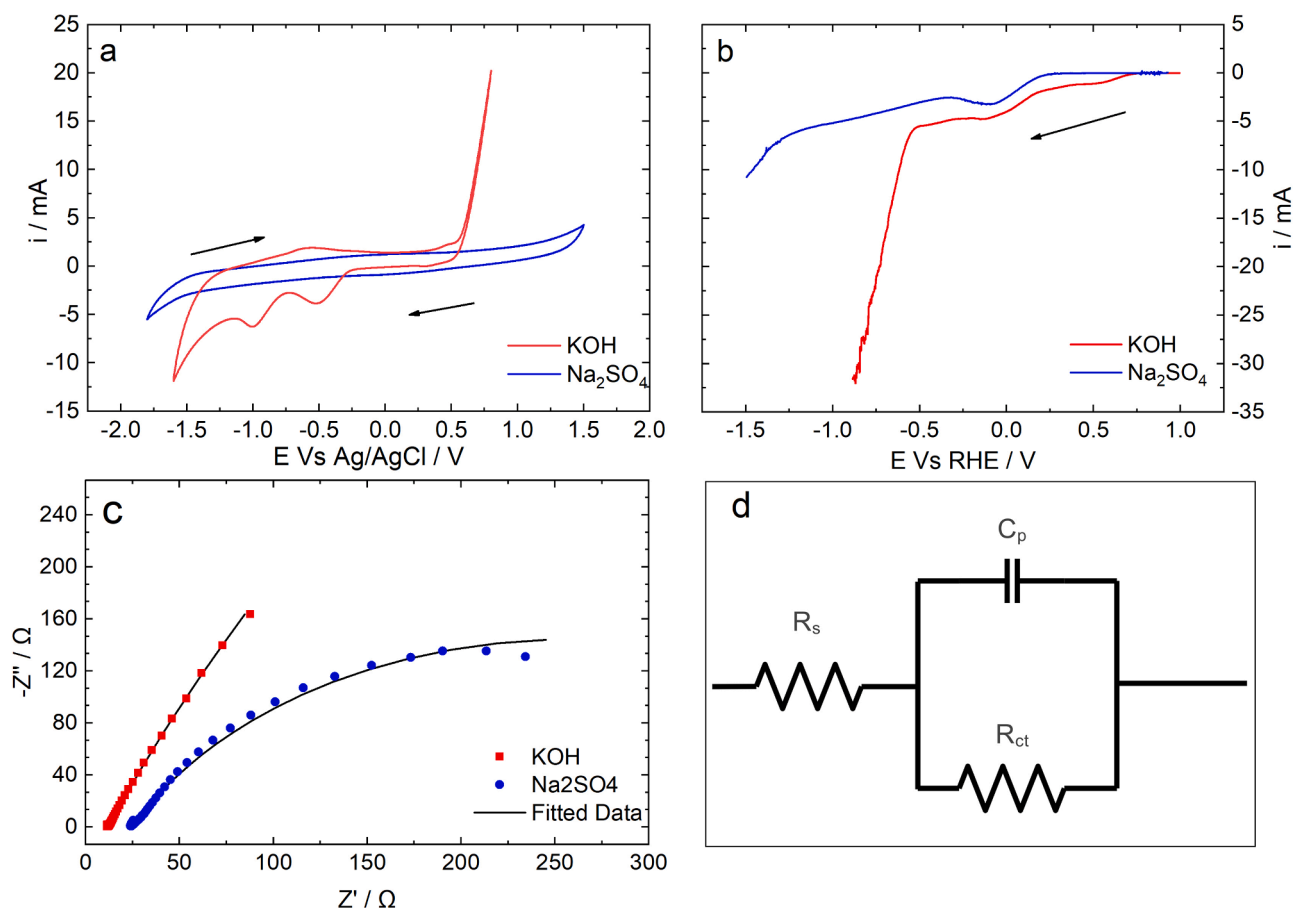
Fig. 8. (a) Cyclic voltammetry of the HEA/g-40 electrode performed at a scan rate of 50 mV s^{-1} in Na$_2$SO$_4$ (pH 5) and KOH (pH 14). (b) Linear scan voltammetry at 1 mV s^{-1} in the cathodic direction with representation in the reversible hydrogen potential scale RHE . (c) Nyquist plots at −1.0 V applied potential with AC perturbation $\Delta E = 10$ mV in different solutions. (d) Representation of the equivalent circuit to analyze the EIS data.
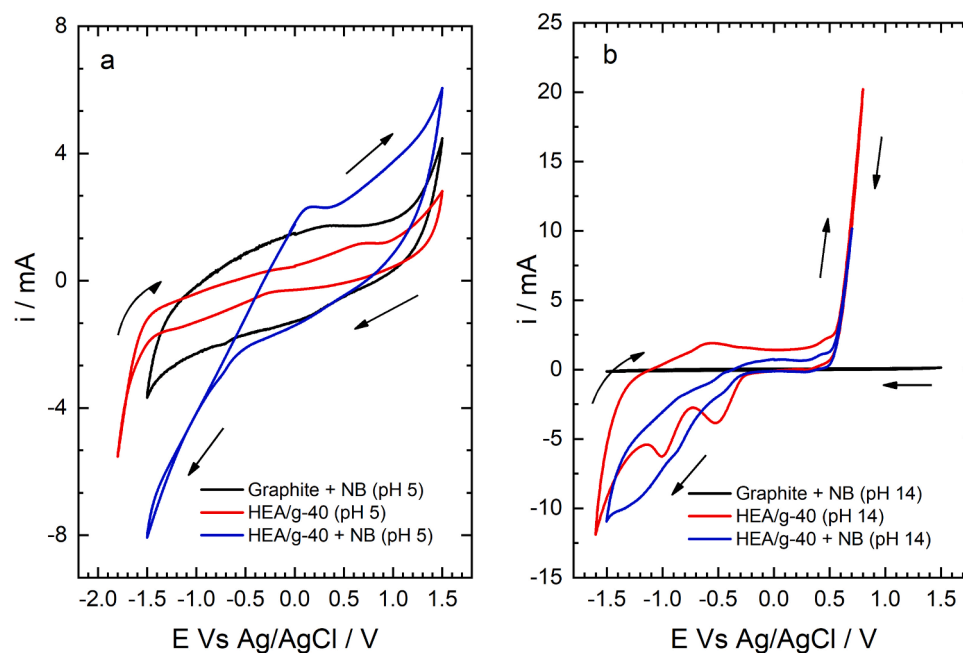
Fig. 9. Cyclic voltammetry of the HEA/g-40 electrode performed at 50 mV s^{-1} with and without nitrobenzene (400 µM) in the electrolyte solutions: (a) 0.1 M Na$_2$SO$_4$ and (b) 1.0 M KOH.

required less energy to take place. The equivalent circuit used to describe the impedance data was a R(RC) circuit as the one shown in Fig. 8d.
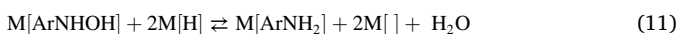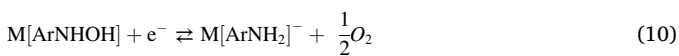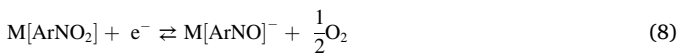
3.3. Nitrobenzene hydrogenation

The hydrogenation of nitrobenzene was used to measure the catalytic activity of the HEA/g-40 electrode. In Fig. 9, we present the effect of adding nitrobenzene (400 μM) to the solution, to evaluate how it affects the surface dynamics of hydrogen adsorption, the surface oxides formation, and their subsequent reduction. Fig. 9a shows an increase in the reduction current when nitrobenzene (NB) was added to the acidic solution starting at 0.8 V. This increase corresponds to the first reduction peak of the surface oxides of the electrode, which means the nitrobenzene rapidly adsorbs in the surface and was reduced once the metal surface was exposed. For applied potential more negative than −0.5 V ($\eta = 0$ V for hydrogen reduction), the current sharply increased, which can be attributed to the irreversible reduction of nitrobenzene involving hydrogen transfer. A similar behavior was observed for Cu electrodes [48–50], thus we can assume that Cu sites actively participate in the nitrobenzene hydrogenation process either by acting as the adsorption site or by providing the adsorbed hydrogen species required for the hydrogenation process.

In the positive scan direction, an oxidation signal appeared at 0 V, which was attributed to the reversible oxidation of reduced nitrobenzene where hydrogen transfer was not involved yet. Finally, a wider signal was observed above 0.2 V overlapping the oxygen evolution signal, which was attributed to the oxidation of reduced species coming from the reduction of nitrobenzene, and the formation of surface oxides of the alloy [77,93–96].

The electrochemistry in alkaline medium (KOH) was rather different than in acidic medium. Fig. 9b shows how the first reduction signal of the alloy (−0.5 V) was drastically reduced at pH 14, while there was an increase in the reduction signal afterward, overlapping with the second reduction signal of the alloy (−1.0 V). This was attributed to the strong adsorption of the nitrobenzene on the surface and the competition with the water molecules (H$_2$ precursors) for the active sites. This strong adsorption and subsequent competition also hindered the surface oxidation of the electrode, which caused the loss or decrease in the oxidation signals of the electrode at positive potentials. These results also imply that the reversible direct reduction of the nitrobenzene was unfavored, and that the hydrogenation mechanism was favored during the nitrobenzene conversion.

The electrochemical hydrogenation mechanism of nitrobenzene has been extensively studied on single metals or simple alloys [50]. The following surface reactions of nitrobenzene must be considered Eqs. (7)-(12):

$$ArNO_2 + M[\,] \rightleftarrows M[ArNO_2] \tag{7}$$

$$M[ArNO_2] + e^- \rightleftarrows M[ArNO]^- + \frac{1}{2}O_2 \tag{8}$$

$$M[ArNO]^- + e^- + 2H_2O \rightleftarrows M[ArNHOH] + 2OH^- \tag{9}$$

$$M[ArNHOH] + e^- \rightleftarrows M[ArNH_2]^- + \frac{1}{2}O_2 \tag{10}$$

$$M[ArNHOH] + 2M[H] \rightleftarrows M[ArNH_2] + 2M[\,] + H_2O \tag{11}$$

$$M[ArNH_2] \rightleftarrows ArNH_2 + M[\,] \tag{12}$$

where ArNO$_2$, ArNO, ArNHOH and ArNH$_2$ refer to nitrobenzene, nitrosobenzene, phenylhydroxylamine and aniline, respectively. All the individual reduction signals were observed in the cyclic voltammetry in basic pH (KOH) (Fig 9b), a small reduction peak at −0.4 V corresponding to the formation of nitrosobenzene, a second peak at −0.6 V to

produce phenylhydroxylamine, and a final signal at −0.9 V corresponding to the direct reduction of aniline [95]. It is important to consider that each reduction product is subject to its own adsorption equilibrium [50], and other indirect reactions can take place in the liquid phase, which may affect the final products concentration but are irrelevant to the electrochemical signals obtained [50]. In this series of equations, Eq. (10) is fundamental for our analysis since it directly relates the aniline production to the surface concentration of hydrogen atoms. In this case, we can assume that any changes in the Tafel slopes of the hydrogen evolution process are caused by the competition for the active sites between -H and the organic species, this at sufficiently high overpotentials where the controlling process is the H$_2$ evolution.

When comparing the Tafel slopes in both conditions (acid and alkaline pH with no nitrobenzene), a remarkable difference was observed (Fig. 10). The results showed a slope of 320 mV in alkaline medium meaning the hydrogen evolution reaction can be controlled by the Volmer reaction, and the surface coverage is the rate-limiting factor. In the case of the acidic medium, a much higher slope of 4413 mV was obtained, which implies the hydrogen evolution process was not controlled by the hydrogen reduction mechanisms (Volmer-Tafel, Volmer-Heyrovsky) but most likely controlled by diffusion, or a much higher voltage input is required to achieve proper activation of the adsorbed species.

In Fig. 10, the Tafel slopes of the hydrogen evolution region showed how the presence of nitrobenzene affected the surface dynamics of the adsorbed species. In acidic medium (Na$_2$SO$_4$), the slope decreased from 4413 mV to 1023 mV, corresponding to the observed increase in the current from the cyclic voltammetry. This change means that there is a direct reduction of nitrobenzene taking place and there was little competition for the active sites to produce the adsorbed species (-H and -OONC$_6$H$_5$). This strong effect on the current by the applied potential indicates that at low overpotentials, where hydrogen evolution is still slow, the direct reduction of NB was the most favored process, while at higher overpotentials, the hydrogenation process became more important despite of the massive hydrogen evolution that significantly increased under this condition.

In the case of the alkaline medium (KOH), the effect seemed to be opposite to that in acidic medium, namely the hydrogen evolution slope became larger (from 320 mV to 1454 mV), meaning there was a decrease in the effect of the applied overpotential. This was attributed to the strong adsorption and competition between the water molecules (-OH$_2$) and the nitrobenzene (-OONC$_6$H$_5$) for the active sites. This competition decreased the surface concentration of water molecules, reducing the
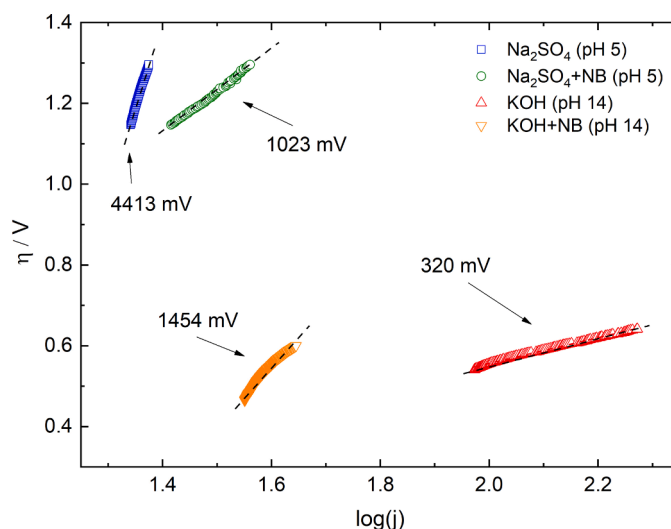

Fig. 10. Tafel slopes for the HEA/g-40 electrode in different electrolytes with and without nitrobenzene (400 μM).

conversion rate of nitrobenzene to aniline. On the other hand, no direct reduction of nitrobenzene was observed, implying that only the hydrogen transfer reaction was responsible for the reduction of nitrobenzene. This competition and co-dependence on the surface coverage could lead to lower activity of nitrobenzene conversion, but also a higher selectivity towards extensively hydrogenated species.

To measure the catalytic effect of the HEA electrode on the nitrobenzene hydrogenation, different applied potentials were used, and the concentration of nitrobenzene and aniline were measured as a function of time using UV–vis. A deconvolution was performed to calculate the concentration of each species. The sodium sulfate medium (pH 5) was chosen to study the effect of the applied potential, owing to the biggest potential range available before the HER becomes the main reaction. Fig. 11a-b shows the concentrations of nitrobenzene (NB) and aniline (AN), respectively, as a function of time at different applied potentials. A linear behavior in NB conversion was observed, meaning the reaction rate was independent of the concentration. This result corroborates the argument of the surface concentration of adsorbed hydrogen (-H) being the rate-limiting factor, therefore, the adsorption equilibrium and surface reactions were the controlling processes. It is important to notice that the conversion decreased as a function of the applied (negative) potential, while the selectivity towards aniline increased going from 21% at −1.0 V to 97% at −2.0 V (see Fig. 11c). This behavior can be explained by the direct hydrogenation of nitrobenzene on the surface without involving hydrogen transfer, favoring the formation of the partially hydrogenated product at lower overpotentials (−1.0 V). In this regard, a byproduct identified as p-nitrophenol was observed when performing the electrolysis at −1.0 V. This can be the result of OH⁻ species produced near the electrode surface after the formation of the

adsorbed -H species that can attack the nucleophilic para position of the nitrobenzene, reducing the selectivity of the process.

In the opposite condition, when the overpotential is high enough to completely activate the hydrogen evolution, the surface hydrogen species are much more active and can attack the nitro group (preferentially adsorbed), favor the extensive hydrogenation, and enlarge the aniline formation. This higher selectivity had a lower conversion rate because most of the electrons are used in the HER, thus resulting in a lower Faradaic efficiency. It is important to note that the reaction rate was not constant in time during the electrolysis. Fig. 11d shows that the aniline production rate or turnover frequency (TOF) decreased in time. As mentioned before, the strong adsorption of the nitrobenzene on the electrode surface hinders the hydrogenation reaction (Eq. (9)), resulting in a rate drop by about 53% at −1.0 V and 60% at −1.5 V. However, if the hydrogen evolution was activated and the amount of hydrogen in the surface was much higher than the concentration of nitrobenzene (i.e., at −2.0 V), the passivation of the electrode was inhibited, and the aniline production rate was only reduced by 10% (Fig. 11d).

The effect of pH was evaluated by comparing the results of the nitrobenzene hydrogenation at both pH conditions. Fig. 12a shows the NB conversion rate and the AN production rate, according to the results previously showed (E_app = −1.0 V). The higher NB conversion rate in the Na₂SO₄ supporting electrolyte was expected since the direct hydrogenation of nitrobenzene was observed which decreased the selectivity and the production of AN. In alkaline medium (KOH), this direct hydrogenation was not possible due to the oxidized surface (Fig. 9b), requiring a more negative potential to activate the hydrogenation process. Fig. 12b shows the conversion and selectivity toward AN production and the results were outstanding, as the selectivity of the process
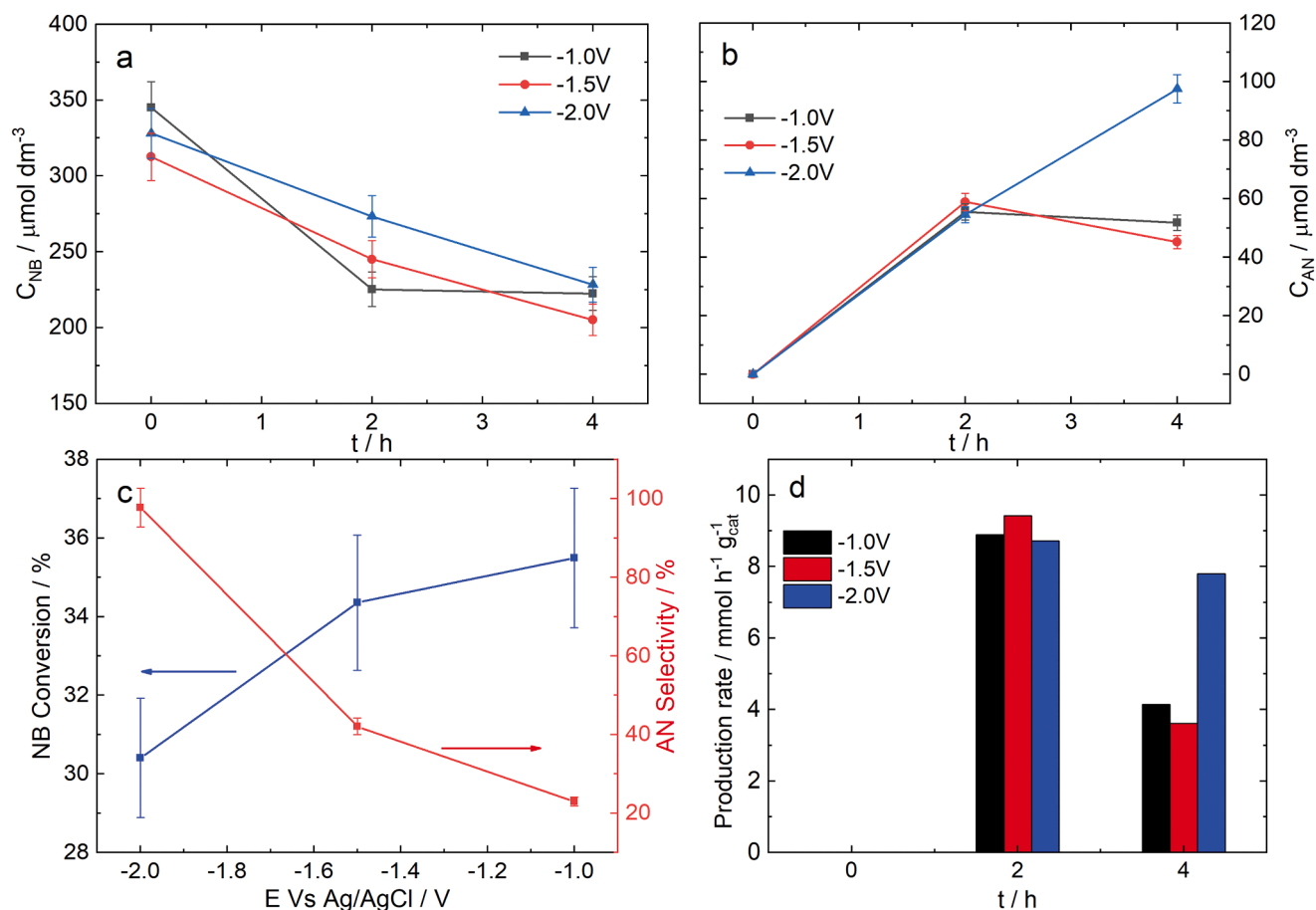
Fig. 11. Concentrations of (a) nitrobenzene and (b) aniline measured during the hydrogenation process in 0.1 M Na₂SO₄ solution at different applied potentials. (c) Conversion and selectivity (towards aniline) at different applied potentials. (d) Aniline production rate as a function of time at different applied potentials.
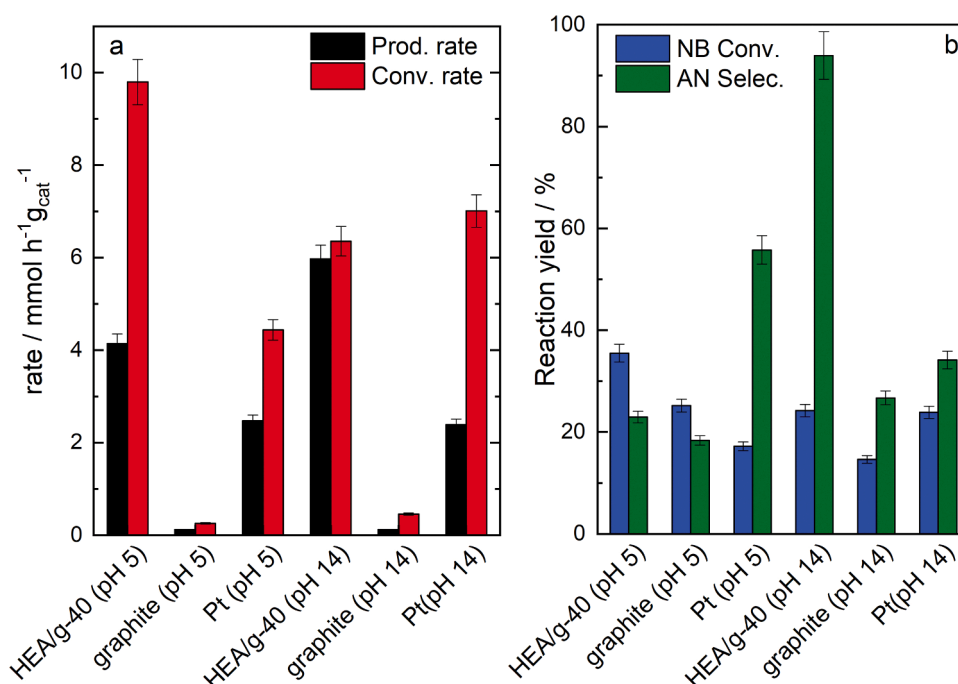
Fig. 12. Comparison of results obtained in different media at $E_{app} = -1.0$ V. (a) Aniline (AN) production and nitrobenzene (NB) conversion rates. (b) NB conversion and AN selectivity. (pH 5 in case of Na_2SO_4 and pH 14 for KOH).

was approximately 93% for the KOH supporting electrolyte, and the conversion was about 24%, surpassing by far the results obtained by a Pt electrode in the same conditions with a selectivity of 34% towards aniline, and a conversion of 23%.

These results are similar to the results obtained at -2.0 V in Na_2SO_4 (conversion 21%, and selectivity 97%). In this regard, it can be concluded that the selectivity of the process is a function of the adsorbed species, i.e. -H and $-OH_2$ for acid and basic media, respectively. This can be better understood when comparing the electrochemical behavior of the electrode in both media (Fig. 8b) represented in the reversible hydrogen scale. This means that at higher pH values, the adsorbed hydrogen species (produced by the electrolysis of water) are more reactive, improving the reaction rates, conversion and selectivity. Only when the massive hydrogen evolution is achieved, at pH 14, the surface has the optimal conditions for improving the reaction selectivity towards AN.

4. Conclusions

In summary, FeCoNiCuZn-based HEAs with homogeneous metal distribution and a single solid solution phase were successfully synthesized on graphite for the first time, to the extent of our knowledge, using a simple, low temperature (30 °C), and low-cost electroless deposition method for catalytic applications. A remarkable activity/weight of the catalyst towards aniline production (6 mmol $g_{cat}^{-1}h^{-1}$) and high selectivity (97%) in alkaline medium make this alloy a promising candidate for extensive conversion processes. The HEA/g-40 showed a capacity to control the products of the reaction as a function of the applied potential between -1.0 and -2.0 V in Na_2SO_4 solution. The HEA showed some deactivation over time at lower overpotentials (-1.0 to -1.5 V) likely caused by strong adsorption of nitrobenzene, but higher selectivity and durability when the applied potential was more negative, ascribed to the fast dynamics of surface hydrogen production. A strong dependence of the surface adsorbed hydrogen species (-H), controlled by the applied potential, had a stronger effect than the solution pH on the catalytic performance. Herein, we showed a simple preparation method to obtain a highly functional material, and a

comprehensive methodology to analyze the surface dynamics of the processes involved in multi-step surface reactions catalyzed by applied electrode potential.

Appendix. supplementary materials

Supplementary Information.

Declaration of Competing Interest

The authors declare that they have no known competing financial interests or personal relationships that could have appeared to influence the work reported in this paper.

CRediT authorship contribution statement

Victor Márquez: Conceptualization, Writing – original draft, Investigation. **Janaina S. Santos:** Supervision, Writing – review & editing. **Josephus G. Buijnsters:** Supervision, Writing – review & editing. **Supareak Praserthdam:** Supervision, Writing – review & editing. **Piyasan Praserthdam:** Funding acquisition, Supervision, Writing – review & editing.

Declaration of Competing Interest

The authors declare no conflict of interest.

Acknowledgments

Supplementary materials

Supplementary material associated with this article can be found, in the online version, at doi:10.1016/j.electacta.2022.139972.

References

[1] M.A. Qyyum, R. Dickson, S.F. Ali Shah, H. Niaz, A. Khan, J.J. Liu, M. Lee, Availability, versatility, and viability of feedstocks for hydrogen production: product space perspective, Renew. Sustain. Energy Rev. 145 (2021), 110843, https://doi.org/10.1016/j.rser.2021.110843.

[2] Z. Chen, W. Wei, B.J. Ni, Cost-effective catalysts for renewable hydrogen production via electrochemical water splitting: recent advances, Curr. Opin. Green Sustain. Chem. 27 (2021), 100398, https://doi.org/10.1016/j.cogsc.2020.100398.

[3] D.D. Ma, Q.L. Zhu, MOF-based atomically dispersed metal catalysts: recent progress towards novel atomic configurations and electrocatalytic applications, Coord. Chem. Rev. 422 (2020), 213483, https://doi.org/10.1016/j.ccr.2020.213483.

[4] S. Herwartz, J. Pagenkopf, C. Streuling, Sector coupling potential of wind-based hydrogen production and fuel cell train operation in regional rail transport in berlin and brandenburg, Int. J. Hydrogen Energy (2021), https://doi.org/10.1016/j.ijhydene.2020.11.242.

[5] M. Ramadan, A review on coupling Green sources to Green storage (G2G): case study on solar-hydrogen coupling, Int. J. Hydrogen Energy (2021), https://doi.org/10.1016/j.ijhydene.2020.12.165.

[6] W. Adam, C.R. Saha-Möller, P.A. Ganeshpure, Synthetic applications of nonmetal catalysts for homogeneous oxidations, Chem. Rev. 101 (2001) 3499–3548, https://doi.org/10.1021/cr000019k.

[7] P.H. Matter, U.S. Ozkan, Non-metal catalysts for dioxygen reduction in an acidic electrolyte, Catal. Lett. 109 (2006) 115–123, https://doi.org/10.1007/s10562-006-0067-1.

[8] Y. Zhao, R. Nakamura, K. Kamiya, S. Nakanishi, K. Hashimoto, Nitrogen-doped carbon nanomaterials as non-metal electrocatalysts for water oxidation, Nat. Commun. 4 (2013) 2–8, https://doi.org/10.1038/ncomms3390.

[9] P. Chen, X. Hu, High-efficiency anion exchange membrane water electrolysis employing non-noble metal catalysts, Adv. Energy Mater. 10 (2020) 1–6, https://doi.org/10.1002/aenm.202002285.

[10] X. Mei, J. Xiong, Y. Wei, Y. Zhang, P. Zhang, Q. Yu, Z. Zhao, J. Liu, High-efficient non-noble metal catalysts of 3D ordered macroporous perovskite-type La2NiB'O6 for soot combustion: insight into the synergistic effect of binary Ni and B' sites, Appl. Catal. B Environ. 275 (2020), https://doi.org/10.1016/j.apcatb.2020.119108.

[11] G.S. Kang, J.H. Jang, S.Y. Son, C.H. Lee, Y.K. Lee, D.C. Lee, S.J. Yoo, S. Lee, H.I. Joh, Fe-based non-noble metal catalysts with dual active sites of nanosized metal carbide and single-atomic species for oxygen reduction reaction, J. Mater. Chem. A 8 (2020) 22379–22388, https://doi.org/10.1039/d0ta07748h.

[12] L. Ruan, A. Pei, J. Liao, L. Zeng, G. Guo, K. Yang, Q. Zhou, N. Zhao, L. Zhu, B.H. Chen, Nitrogen-doped carbon nanotubes-supported PdNiCo nanoparticles as a highly efficient catalyst for selective hydrogenation of furfural, Fuel 284 (2021), 119015, https://doi.org/10.1016/j.fuel.2020.119015.

[13] W. Xiong, Z. Wang, S. He, F. Hao, Y. Yang, Y. Lv, W. Zhang, P. Liu, H. Luo, Nitrogen-doped carbon nanotubes as a highly active metal-free catalyst for nitrobenzene hydrogenation, Appl. Catal. B Environ. 260 (2020), 118105, https://doi.org/10.1016/j.apcatb.2019.118105.

[14] G. Hong, Y. Chen, P. Li, J. Zhang, Controlling the growth of single-walled carbon nanotubes on surfaces using metal and non-metal catalysts, Carbon N. Y. 50 (2012) 2067–2082, https://doi.org/10.1016/j.carbon.2012.01.035.

[15] J. Zhu, C. He, Y. Li, S. Kang, P.K. Shen, One-step synthesis of boron and nitrogen-dual-self-doped graphene sheets as non-metal catalysts for oxygen reduction reaction, J. Mater. Chem. A 1 (2013) 14700–14705, https://doi.org/10.1039/c3ta13318d.

[16] E. Marinho, P.A. da Silva Autreto, Me-graphane: tailoring the structural and electronic properties of Me-grapheneviahydrogenation, Phys. Chem. Chem. Phys. 23 (2021) 9483–9491, https://doi.org/10.1039/d0cp06684b.

[17] S. Li, J. Li, Y. Wang, C. Yu, Y. Li, W. Duan, Y. Wang, J. Zhang, Large transport gap modulation in graphene via electric-field-controlled reversible hydrogenation, Nat. Electron. 4 (2021) 254–260, https://doi.org/10.1038/s41928-021-00548-2.

[18] J. Wang, Q. Wei, Q. Ma, Z. Guo, F. Qin, Z.R. Ismagilov, W. Shen, Constructing Co@ N-doped graphene shell catalyst via Mott-Schottky effect for selective hydrogenation of 5-hydroxylmethylfurfural, Appl. Catal. B Environ. 263 (2020), 118339, https://doi.org/10.1016/j.apcatb.2019.118339.

[19] Q. Liu, J. Shen, X. Yu, X. Yang, W. Liu, J. Yang, H. Tang, H. Xu, H. Li, Y. Li, J. Xu, Unveiling the origin of boosted photocatalytic hydrogen evolution in simultaneously (S, P, O)-Codoped and exfoliated ultrathin g-C3N4 nanosheets, Appl. Catal. B Environ. 248 (2019) 84–94, https://doi.org/10.1016/j.apcatb.2019.02.020.

[20] A. Mishra, A. Mehta, S. Basu, N.P. Shetti, K.R. Reddy, T.M. Aminabhavi, Graphitic carbon nitride (g–C3N4)–based metal-free photocatalysts for water splitting: a review, Carbon N. Y. 149 (2019) 693–721, https://doi.org/10.1016/j.carbon.2019.04.104.

[21] L. Shabnam, S.N. Faisal, V.C. Hoang, A. Martucci, V.G. Gomes, Doping reduced graphene oxide and graphitic carbon nitride hybrid for dual functionality: high performance supercapacitance and hydrogen evolution reaction, J. Electroanal. Chem. 856 (2020), 113503, https://doi.org/10.1016/j.jelechem.2019.113503.

[22] Y. Wang, S. Zhao, Y. Zhang, W. Chen, S. Yuan, Y. Zhou, Z. Huang, Synthesis of graphitic carbon nitride with large specific surface area via copolymerizing with nucleobases for photocatalytic hydrogen generation, Appl. Surf. Sci. (2018), https://doi.org/10.1016/j.apsusc.2018.08.215.

[23] M.K. Kesarla, N.N. Kumar Reddy, F. Ortiz-Chi, C.G. Espinosa-González, J.G. Torres Torres, N. Hernandez-Como, S. Godavarthi, L. Martínez-Gómez, Transformation of g-C3N4 into onion like carbon on nickel nanoparticles for ultrafast hydrogenation, Mater. Chem. Phys. 240 (2020), https://doi.org/10.1016/j.matchemphys.2019.122157.

[24] C.J. Kaminsky, J. Wright, Y. Surendranath, Graphite-conjugation enhances porphyrin electrocatalysis, ACS Catal. 9 (2019) 3667–3671, https://doi.org/10.1021/acscatal.9b00404.

[25] B. Cantor, I.T.H. Chang, P. Knight, A.J.B. Vincent, Microstructural development in equiatomic multicomponent alloys, Mater. Sci. Eng. A 375–377 (2004) 213–218, https://doi.org/10.1016/j.msea.2003.10.257.

[26] J.W. Yeh, S.K. Chen, S.J. Lin, J.Y. Gan, T.S. Chin, T.T. Shun, C.H. Tsau, S.Y. Chang, Nanostructured high-entropy alloys with multiple principal elements: novel alloy design concepts and outcomes, Adv. Eng. Mater. 6 (2004) 299–303, https://doi.org/10.1002/adem.200300567.

[27] M.H. Tsai, J.W. Yeh, High-entropy alloys: a critical review, Mater. Res. Lett. 2 (2014) 107–123, https://doi.org/10.1080/21663831.2014.912690.

[28] S. Wang, H. Xin, Predicting catalytic activity of high-entropy alloys for electrocatalysis, Chemistry 5 (2019) 502–504, https://doi.org/10.1016/j.chempr.2019.02.015.

[29] X. Wang, W. Guo, Y. Fu, High-entropy alloys: emerging materials for advanced functional applications, J. Mater. Chem. A 9 (2021) 663–701, https://doi.org/10.1039/d0ta09601f.

[30] X. Xu, Y. Guo, B.P. Bloom, J. Wei, H. Li, H. Li, Y. Du, Z. Zeng, L. Li, D.H. Waldeck, Elemental core level shift in high entropy alloy nanoparticles via X-ray photoelectron spectroscopy analysis and first-principles calculation, ACS Nano 14 (2020) 17704–17712, https://doi.org/10.1021/acsnano.0c09470.

[31] W. Zhang, P.K. Liaw, Y. Zhang, Science and technology in high-entropy alloys, Sci. China Mater. 61 (2018) 2–22, https://doi.org/10.1007/s40843-017-9195-8.

[32] D. Wu, K. Kusada, T. Yamamoto, T. Toriyama, S. Matsumura, I. Gueye, O. Seo, J. Kim, S. Hiroi, O. Sakata, S. Kawaguchi, Y. Kubota, H. Kitagawa, On the electronic structure and hydrogen evolution reaction activity of platinum group metal-based high-entropy-alloy nanoparticles, Chem. Sci. 11 (2020) 12731–12736, https://doi.org/10.1039/d0sc02351e.

[33] D. Karlsson, G. Ek, J. Cedervall, C. Zlotea, K.T. Møller, T.C. Hansen, J. Bednarčík, M. Paskevicius, M.H. Sørby, T.R. Jensen, U. Jansson, M. Sahlberg, Structure and hydrogenation properties of a HfNbTiVZr high-entropy alloy, Inorg. Chem. 57 (2018) 2103–2110, https://doi.org/10.1021/acs.inorgchem.7b03004.

[34] Q. Yang, G. Wang, H. Wu, B.A. Beshiwork, D. Tian, S. Zhu, Y. Yang, X. Lu, Y. Ding, Y. Ling, Y. Chen, B. Lin, A high-entropy perovskite cathode for solid oxide fuel cells, J. Alloys Compd. 872 (2021), 159633, https://doi.org/10.1016/j.jallcom.2021.159633.

[35] J. Huang, K. Du, P. Wang, H. Yin, D. Wang, Electrochemical preparation and homogenization of face-centered FeCoNiCu medium entropy alloy electrodes enabling oxygen evolution reactions, Electrochim. Acta 378 (2021), 138142, https://doi.org/10.1016/j.electacta.2021.138142.

[36] D. Zhang, H. Zhao, X. Wu, Y. Deng, Z. Wang, Y. Han, H. Li, Y. Shi, X. Chen, S. Li, J. Lai, B. Huang, L. Wang, Multi-site electrocatalysts boost pH-universal nitrogen reduction by high-entropy alloys, Adv. Funct. Mater. 31 (2021) 1–8, https://doi.org/10.1002/adfm.202006939.

[37] A. Eftekhari, Electrocatalysts for hydrogen evolution reaction, Int. J. Hydrogen Energy 42 (2017) 11053–11077, https://doi.org/10.1016/j.ijhydene.2017.02.125.

[38] K.V. Yusenko, S. Riva, P.A. Carvalho, M.V. Yusenko, S. Arnaboldi, A.S. Sukhikh, M. Hanfland, S.A. Gromilov, First hexagonal close packed high-entropy alloy with outstanding stability under extreme conditions and electrocatalytic activity for methanol oxidation, Scr. Mater. 138 (2017) 22–27, https://doi.org/10.1016/j.scriptamat.2017.05.022.

[39] X. Cui, B. Zhang, C. Zeng, S. Guo, Electrocatalytic activity of high-entropy alloys toward oxygen evolution reaction, MRS Commun. 8 (2018) 1230–1235, https://doi.org/10.1557/mrc.2018.111.

[40] S. Li, X. Tang, H. Jia, H. Li, G. Xie, X. Liu, X. Lin, H.J. Qiu, Nanoporous high-entropy alloys with low Pt loadings for high-performance electrochemical oxygen reduction, J. Catal. 383 (2020) 164–171, https://doi.org/10.1016/j.jcat.2020.01.024.

[41] M. Ghadiri, A. Hemmati, M. Rezakazemi, Numerical investigation of ethylbenzene dehydrogenation and nitrobenzene hydrogenation in a membrane reactor: effect of operating conditions, Int. J. Hydrogen Energy 46 (2021) 28641–28656, https://doi.org/10.1016/j.ijhydene.2021.06.100.

[42] Á. Prekob, M. Udayakumar, G. Karacs, F. Kristály, G. Muránszky, A.K. Leskó, Z. Németh, B. Viskolcz, L. Vanyorek, Development of highly efficient, glassy carbon foam supported, palladium catalysts for hydrogenation of nitrobenzene, Nanomaterials 11 (2021) 1172, https://doi.org/10.3390/nano11051172.

[43] A. Khazayialiabad, D. Iranshahi, S. Ebrahimian, A conceptual evaluation of a new multifunctional reactor containing glycerol steam reforming and nitrobenzene hydrogenation, Chem. Eng. Process. - Process Intensif. 164 (2021), 108405, https://doi.org/10.1016/j.cep.2021.108405.

[44] F. Tong, X. Liang, F. Ma, X. Bao, Z. Wang, Y. Liu, P. Wang, H. Cheng, Y. Dai, B. Huang, Z. Zheng, Plasmon-mediated nitrobenzene hydrogenation with formate as the hydrogen donor studied at a single-particle level, ACS Catal. 11 (2021) 3801–3809, https://doi.org/10.1021/acscatal.1c00164.

[45] Y. Xie, D. Liu, B. Wang, D. Li, Z. Yan, Y. Chen, J. Shen, Z. Zhang, X. Wang, Monolayer Bi2W1- xMo xO6 solid solutions for structural polarity to boost

V. Márquez et al.

Electrochimica Acta 410 (2022) 139972

photocatalytic reduction of nitrobenzene under visible light, ACS Sustain. Chem. Eng. 9 (2021) 2465–2474, https://doi.org/10.1021/acssuschemeng.0c07324.

[46] Y. Zhao, C. Liu, C. Wang, X. Chong, B. Zhang, Sulfur vacancy-promoted highly selective electrosynthesis of functionalized aminoarenes via transfer hydrogenation of nitroarenes with H2O over a Co3S4−x nanosheet cathode, CCS Chem. 3 (2021) 507–515, https://doi.org/10.31635/ccschem.020.202000218.

[47] M. Jin, Y. Liu, X. Zhang, J. Wang, S. Zhang, G. Wang, Y. Zhang, H. Yin, H. Zhang, H. Zhao, Selective electrocatalytic hydrogenation of nitrobenzene over copper-platinum alloying catalysts: experimental and theoretical studies, Appl. Catal. B Environ. 298 (2021), 120545, https://doi.org/10.1016/j.apcatb.2021.120545.

[48] J. Jiang, R. Zhai, X. Bao, Electrocatalytic properties of Cu-Zr amorphous alloy towards the electrochemical hydrogenation of nitrobenzene, J. Alloys Compd. (2003) 248–258, https://doi.org/10.1016/S0925-8388(02)01359-2.

[49] Z. Yin, Y. Xiao, X. Wan, Y. Jiang, G. Chen, Q. Shi, S. Cao, High photocatalytic activity of Cu2O embedded in hierarchically hollow SiO2 for efficient chemoselective hydrogenation of nitroarenes, J. Mater. Sci. 56 (2021) 3874–3886, https://doi.org/10.1007/s10853-020-05449-x.

[50] B. Wouters, X. Sheng, A. Boschin, T. Breugelman, E. Ahlberg, I.F.J. Vankelecom, P. P. Pescarmona, A. Hubin, The electrocatalytic behaviour of Pt and Cu nanoparticles supported on carbon nanotubes for the nitrobenzene reduction in ethanol, Electrochim. Acta 111 (2013) 405–410, https://doi.org/10.1016/j.electacta.2013.07.210.

[51] J. Song, Z.F. Huang, L. Pan, K. Li, X. Zhang, L. Wang, J.J. Zou, Review on selective hydrogenation of nitroarene by catalytic, photocatalytic and electrocatalytic reactions, Appl. Catal. B Environ. 227 (2018) 386–408, https://doi.org/10.1016/j.apcatb.2018.01.052.

[52] M.E. Björketun, A.S. Bondarenko, B.L. Abrams, I. Chorkendorff, J. Rossmeisl, Screening of electrocatalytic materials for hydrogen evolution, Phys. Chem. Chem. Phys. 12 (2010) 10536–10541, https://doi.org/10.1039/c003826c.

[53] M. Zhao, H. Tang, Q. Yang, Y. Gu, H. Zhu, S. Yan, Z. Zou, Inhibiting hydrogen evolution using a chloride adlayer for efficient electrochemical CO2 reduction on Zn electrodes, ACS Appl. Mater. Interfaces 12 (2020) 4565–4571, https://doi.org/10.1021/acsami.9b22811.

[54] C. González-Buch, I. Herraiz-Cardona, E. Ortega, J. García-Antón, V. Pérez-Herranz, Synthesis and characterization of macroporous Ni, Co and Ni-Co electrocatalytic deposits for hydrogen evolution reaction in alkaline media, Int. J. Hydrogen Energy 38 (2013) 10157–10169, https://doi.org/10.1016/j.ijhydene.2013.06.016.

[55] S. Li, X. Yang, S. Yang, Q. Gao, S. Zhang, X. Yu, Y. Fang, S. Yang, X. Cai, An amorphous trimetallic (Ni-Co-Fe) hydroxide-sheathed 3D bifunctional electrode for superior oxygen evolution and high-performance cable-type flexible zinc-air batteries, J. Mater. Chem. A 8 (2020) 5601–5611, https://doi.org/10.1039/d0ta00888e.

[56] C. Larson, J.R. Smith, Recent trends in metal alloy electrolytic and electroless plating research: a review, Trans. Inst. Met. Finish. 89 (2011) 333–341, https://doi.org/10.1179/174591911X13171174481239.

[57] F. Li, Y. Li, Q. Zhuo, D. Zhou, Y. Zhao, Z. Zhao, X. Wu, Y. Shan, L. Sun, Electroless plating of NiFeP alloy on the surface of silicon photoanode for efficient photoelectrochemical water oxidation, ACS Appl. Mater. Interfaces 12 (2020) 11479–11488, https://doi.org/10.1021/acsami.9b19418.

[58] B. Veeraraghavan, H. Kim, B. Popov, Optimization of electroless Ni-Zn-P deposition process: experimental study and mathematical modeling, Electrochim. Acta 49 (2004) 3143–3154, https://doi.org/10.1016/j.electacta.2004.01.035.

[59] P. Pip, C. Donnelly, M. Döbeli, C. Gunderson, L.J. Heyderman, L. Philippe, Electroless deposition of Ni–Fe alloys on scaffolds for 3D nanomagnetism, Small 16 (2020) 3–6, https://doi.org/10.1002/smll.202004099.

[60] R.K. Pandey, L. Chen, S. Teraji, H. Nakanishi, S. Noh, Eco-friendly, direct deposition of metal nanoparticles on graphite for electrochemical energy conversion and storage, ACS Appl. Mater. Interfaces 11 (2019) 36525–36534, https://doi.org/10.1021/acsami.9b09273.

[61] J. Huang, P. Wang, P. Li, H. Yin, D. Wang, Regulating electrolytic Fe0.5CoNiCuZnx high entropy alloy electrodes for oxygen evolution reactions in alkaline solution, J. Mater. Sci. Technol. 93 (2021) 110–118, https://doi.org/10.1016/j.jmst.2021.03.046.

[62] V. Ramasamy, G. Vijayalakshmi, Effect of Zn doping on structural, optical and thermal properties of CeO2 nanoparticles, Superlattices Microstruct. 85 (2015) 510–521, https://doi.org/10.1016/j.spmi.2015.05.015.

[63] V.G. Patil, S.E. Shirsath, S.D. More, S.J. Shukla, K.M. Jadhav, Effect of zinc substitution on structural and elastic properties of cobalt ferrite, J. Alloys Compd. 488 (2009) 199–203, https://doi.org/10.1016/j.jallcom.2009.08.078.

[64] V.K. Soni, S. Sanyal, S.K. Sinha, Investigation of phase stability of novel equiatomic FeCoNiCuZn based-high entropy alloy prepared by mechanical alloying, AIP Conf. Proc. 1953 (2018), https://doi.org/10.1063/1.5032588.

[65] A.G. Shard, X-ray Photoelectron Spectroscopy, Elsevier Inc., 2019, https://doi.org/10.1016/B978-0-12-814182-3.00019-5.

[66] P.S. Bagus, E.S. Ilton, C.J. Nelin, The interpretation of XPS spectra: insights into materials properties, Surf. Sci. Rep. 68 (2013) 273–304, https://doi.org/10.1016/j.surfrep.2013.03.001.

[67] P.S. Bagus, C.J. Nelin, C.R. Brundle, B.V. Crist, N. Lahiri, K.M. Rosso, Covalency in Fe2O3 and FeO: consequences for XPS satellite intensity, J. Chem. Phys. 153 (2020), https://doi.org/10.1063/5.0030350.

[68] P.S. Bagus, E. Ilton, C.J. Nelin, Extracting chemical information from XPS spectra: a perspective, Catal. Lett. 148 (2018) 1785–1802, https://doi.org/10.1007/s10562-018-2417-1.

[69] A. Claypole, J. Claypole, T. Claypole, D. Gethin, L. Kilduff, The effect of plasma functionalization on the print performance and time stability of graphite

[70] nanoplatelet electrically conducting inks, J. Coat. Technol. Res. 18 (2021) 193–203, https://doi.org/10.1007/s11998-020-00414-4.

[70] M. Trought, I. Wentworth, T. Leftwich, K. Perrine, Effects of wet chemical oxidation on surface functionalization and morphology of highly oriented pyrolytic graphite, ChemRxiv (2020) 1–32, https://doi.org/10.26434/chemrxiv.12907604.v1.

[71] N.R. Ostyn, B. Thijs, J.A. Steele, S.P. Sree, W. Wangermez, J. Teyssandier, M. M. Minjauw, J. Li, C. Detavernier, M.B.J. Roeffaers, S. De Feyter, J.A. Martens, Controlled graphite surface functionalization using contact and remote photocatalytic oxidation, Carbon N. Y. 172 (2021) 637–646, https://doi.org/10.1016/j.carbon.2020.10.069.

[72] Y. Zhu, C. Huang, C. Li, M. Fan, K. Shu, H.C. Chen, Strong synergetic electrochemistry between transition metals of A phase Ni−Co−Mn hydroxide contributed superior performance for hybrid supercapacitors, J. Power Sources 412 (2019) 559–567, https://doi.org/10.1016/j.jpowsour.2018.11.080.

[73] T.C. Chou, C.C. Chang, H.L. Yu, W.Y. Yu, C.L. Dong, J.J. Velasco-Vélez, C. H. Chuang, L.C. Chen, J.F. Lee, J.M. Chen, H.L. Wu, Controlling the oxidation state of the Cu electrode and reaction intermediates for electrochemical CO2 reduction to ethylene, J. Am. Chem. Soc. 142 (2020) 2857–2867, https://doi.org/10.1021/jacs.9b11126.

[74] Y.X. Chen, S.P. Chen, Z.Y. Zhou, N. Tian, Y.X. Jiang, S.G. Sun, Y. Ding, L.W. Zhong, Tuning the shape and catalytic activity of Fe nanocrystals from rhombic dodecahedra and tetragonal bipyramids to cubes by electrochemistry, J. Am. Chem. Soc. 131 (2009) 10860–10862, https://doi.org/10.1021/ja904225q.

[75] Y. Zhang, Z. Chen, H. Qiu, W. Yang, Z. Zhao, J. Zhao, G. Cui, Pursuit of reversible Zn electrochemistry: a time-honored challenge towards low-cost and green energy storage, NPG Asia Mater. 12 (2020) 1–24, https://doi.org/10.1038/s41427-019-0167-1.

[76] K.K. Lee, W.S. Chin, C.H. Sow, Cobalt-based compounds and composites as electrode materials for high-performance electrochemical capacitors, J. Mater. Chem. A. 2 (2014) 17212–17248, https://doi.org/10.1039/c4ta02074j.

[77] R.L. Doyle, I.J. Godwin, M.P. Brandon, M.E.G. Lyons, Redox and electrochemical water splitting catalytic properties of hydrated metal oxide modified electrodes, Phys. Chem. Chem. Phys. 15 (2013) 13737–13783, https://doi.org/10.1039/c3cp51213d.

[78] T. Erdey-Grúz, M. Volmer, Zur theorie der wasserstoff überspannung, Z. Phys. Chem. 150A (1930) 203–213, https://doi.org/10.1515/zpch-1930-15020.

[79] J. Tafel, Über die Polarisation bei kathodischer Wasserstoffentwicklung, Z. Phys. Chem. 50 (1905) 641–712, https://doi.org/10.1515/zpch-1905-5043.

[80] S. Trasatti, Work function, electronegativity, and electrochemical behaviour of metals. III. Electrolytic hydrogen evolution in acid solutions, J. Electroanal. Chem. 39 (1972) 163–184, https://doi.org/10.1016/S0022-0728(72)80485-6.

[81] G. Zhao, K. Rui, S.X. Dou, W. Sun, Heterostructures for electrochemical hydrogen evolution reaction: a review, Adv. Funct. Mater. 28 (2018) 1–26, https://doi.org/10.1002/adfm.201803291.

[82] F. Safizadeh, E. Ghali, G. Houlachi, Electrocatalysis developments for hydrogen evolution reaction in alkaline solutions - a review, Int. J. Hydrogen Energy 40 (2015) 256–274, https://doi.org/10.1016/j.ijhydene.2014.10.109.

[83] T. Löffler, A. Savan, H. Meyer, M. Meischein, V. Strotkötter, A. Ludwig, W. Schuhmann, Design of complex solid-solution electrocatalysts by correlating configuration, adsorption energy distribution patterns, and activity curves, Angew. Chem. Int. Ed. 59 (2020) 5844–5850, https://doi.org/10.1002/anie.201914666.

[84] G.M. Tomboc, T. Kwon, J. Joo, K. Lee, High entropy alloy electrocatalysts: a critical assessment of fabrication and performance, J. Mater. Chem. A 8 (2020) 14844–14862, https://doi.org/10.1039/d0ta05176d.

[85] V.A. Saveleva, L. Wang, D. Teschner, T. Jones, A.S. Gago, K.A. Friedrich, S. Zafeiratos, R. Schlögl, E.R. Savinova, Operando evidence for a universal oxygen evolution mechanism on thermal and electrochemical iridium oxides, J. Phys. Chem. Lett. 9 (2018) 3154–3160, https://doi.org/10.1021/acs.jpclett.8b00810.

[86] E. Fabbri, T.J. Schmidt, Oxygen evolution reaction - the enigma in water electrolysis, ACS Catal. 8 (2018) 9765–9774, https://doi.org/10.1021/acscatal.8b02712.

[87] P. Rasiyah, A.C.C. Tseung, A mechanistic study of oxygen evolution on NiCo2O4 : II. Electrochemical kinetics, J. Electrochem. Soc. 130 (1983) 2384–2386, https://doi.org/10.1149/1.2119592.

[88] C. Gabrielli, P.P. Grand, A. Lasia, H. Perrot, Investigation of hydrogen adsorption-absorption into thin palladium films, J. Electrochem. Soc. 151 (2004) A1925, https://doi.org/10.1149/1.1797033.

[89] H. Duncan, A. Lasia, Mechanism of hydrogen adsorption/absorption at thin Pd layers on Au(1 1 1), Electrochim. Acta 52 (2007) 6195–6205, https://doi.org/10.1016/j.electacta.2007.03.068.

[90] R.Q. Yao, Y.T. Zhou, H. Shi, W. Bin Wan, Q.H. Zhang, L. Gu, Y.F. Zhu, Z. Wen, X. Y. Lang, Q. Jiang, Nanoporous surface high-entropy alloys as highly efficient multisite electrocatalysts for nonacidic hydrogen Evolution reaction, Adv. Funct. Mater. 31 (2021) 1–9, https://doi.org/10.1002/adfm.202009613.

[91] M. Liu, Z. Zhang, F. Okejiri, S. Yang, S. Zhou, S. Dai, Entropy-maximized synthesis of multimetallic nanoparticle catalysts via a ultrasonication-assisted wet chemistry method under ambient conditions, Adv. Mater. Interfaces 6 (2019) 1–6, https://doi.org/10.1002/admi.201900015.

[92] R.K. Singh, A. Schechter, Electrochemical investigation of urea oxidation reaction on β Ni(OH)2 and Ni/Ni(OH)2, Electrochim. Acta 278 (2018) 405–411, https://doi.org/10.1016/j.electacta.2018.05.049.

[93] W.H. Smith, A.J. Bard, Electrochemical reactions of organic compounds in liquid ammonia. III. reductive alkylation of quinoline, J. Am. Chem. Soc. 97 (1975) 6491–6495, https://doi.org/10.1021/ja00855a034.

[94] J. Marquez, D. Pletcher, A study of the electrochemical reduction of nitrobenzene to p-aminophenol, J. Appl. Electrochem. 10 (1980) 567–573, https://doi.org/10.1007/BF00615477.

[95] Y.P. Li, H. Bin Cao, C.M. Liu, Y. Zhang, Electrochemical reduction of nitrobenzene at carbon nanotube electrode, J. Hazard. Mater. 148 (2007) 158–163, https://doi.org/10.1016/j.jhazmat.2007.02.021.

[96] D.S. Silvester, A.J. Wain, L. Aldous, C. Hardacre, R.G. Compton, Electrochemical reduction of nitrobenzene and 4-nitrophenol in the room temperature ionic liquid [C4dmim][N(T*f*)2], J. Electroanal. Chem. 596 (2006) 131–140, https://doi.org/10.1016/j.jelechem.2006.07.028.